A novel fabrication method of vertically aligned carbon nanotubes by single-stage floating catalyst CVD

B. V.N. Sewwandi[1,2,3*], A. R. Kumarasinghe[3,5], Xing CHEN[1,2,4], P. M.C.J. Bandara[1,2], L. Jayarathna[1,2] and Rohan Weerasooriya[1,2,4]

Abstract

The single-stage floating catalyst chemical vapor deposition (SS-FCCVD) method using the ferrocene route (e.g., ferrocene: catalyst and camphor: carbon source) offers significant but largely unexplored versatility for the production of carbon nanotubes (CNTs). Our study used the SS-FCCVD method to grow vertically aligned carbon nanotubes (VACNTs) on an alumina ceramic reactor surface at 850 °C under a nitrogen atmosphere. The experimental setup included a camphor/ferrocene ratio of 20:1 and a specific temperature gradient of 21 °C/cm. To minimize the catalyst agglomeration, we positioned the chemical sources at a distance of 15 cm from the inlet of the CVD reactor. Alumina ceramic surfaces proved highly effective for VACNT production, showing minimal agglomeration of iron particles, facilitating the formation of reactive sites essential for VACNT growth. The VACNTs grew readily on alumina ceramic surfaces, forming bundled, forest-like structures with segment lengths up to 1.2 mm and diameters around 60 nm. When compared to conventional substrates, the surface area of the reaction zone substrate increases by up to 705%, resulting in a significant boost in VACNT yield. A detailed evaluation of characterization results confirmed the growth mechanism and behavior of Fe particles such that carbon-encapsulated particles are attached to the inner and outer surfaces of the CNTs. These VACNT surfaces exhibited superhydrophobic properties, similar to the lotus leaf effect. The synthesized iron-dispersed CNTs exhibit exceptional efficiency in Chromium (VI) removal, with an impressive adsorption capacity of 0.206 mmol/m^2, positioning them as a promising solution for effective water treatment. This scalable SS-FCCVD method using the ferrocene route achieved the longest VACNTs reported to date.

Keywords Alumina ceramics, Ferrocene, Single-stage floating catalyst chemical vapor deposition, Super-hydrophobic, Vertically aligned carbon nanotube, Chromium removal

*Correspondence:
B. V.N. Sewwandi
niluka.be@nifs.ac.lk
[1]Centre for Water Quality Research, National Institute of Fundamental Studies, Kandy, Sri Lanka
[2]Ministry of Water Supply, China and Sri Lanka Joint Research and Demonstration Centre for Water Technology, Kandy, Sri Lanka
[3]Department of Physics, Faculty of Applied Sciences, University of Sri Jayewardenepura, Nugegoda, Sri Lanka
[4]Key Lab of Aerospace Structural Parts Forming Technology and Equipment of Anhui Province, Institute of and Equipment Technology, Hefei University of Technology, Hefei 230009, PR China
[5]Center for Nanocomposite Research, Faculty of Applied Sciences, University of Sri Jayewardenepura, Nugegoda, Sri Lanka

Introduction

Aligned carbon nanotubes are notable for their unique property enhancements in various applications [1, 2]. The chemical vapor deposition (CVD) methods are highly suitable for the production of vertically aligned carbon nanotubes (VACNTs) due to their safety, easy customization, and scalability. The CNTs and their variants are commonly fabricated by floating catalyst CVD (FC-CVD), using ferrocene-derived Fe^0 nanoparticles as a catalyst and camphor [3–5], toluene [6, 7], or acetylene [8, 9] as carbon sources i.e. ferrocene route. Two-stage or higher CVD configurations are often used to produce VACNTs, yet their adaptation in FC-CVD systems is significantly hindered [10–12].

The morphology of VACNTs is strongly influenced by the size of catalyst nanoparticles and their surface density (2.1×10^{11} cm^{-2}) [13]. Notably, when the catalyst surface roughness is below 15 nm, VACNTs tend to grow with smaller diameters, which promotes vertical alignment due to van der Waals interactions between adjacent nanotubes [14]. When the carbon precursor vaporizes in the external zone, particle coalescence along the FC-CVD tube leads to larger particles (> 15 nm) [15]. Nearly 99% of catalysts remain unutilized due to unsuitable particle size (from Ostwald ripening and amorphous coatings) and catalyst deposition on reactor walls, which reduces active sites [16–18]. Typical double-stage CVD systems yield CNTs only on limited substrate areas (e.g., 10 mm × 10 mm) at the reaction zone, resulting in low yields per operation [19].Floating catalysts reduce aggregation, improving CNT uniformity, while supported catalysts risk diffusion and agglomeration at high temperatures, affecting CNT diameter and alignment. Metal precursors decompose in situ, enhancing catalyst utilization and yield. Also, camphor vapors condense on the connecting tube, hindering their effective delivery to the furnace and causing a significant amount of unreacted chemicals to remain in the flask, ultimately reducing the CNT yield.

To address this challenge, the FC-CVD system needs to be optimized to enhance the morphology and deposition of catalyst particles. Kapoor et al. [20] synthesized metal-filled CNTs using a modified single-step CVD process with camphor as the carbon source and metallocene as the catalyst, growing VACNTs directly on a quartz surface by integrating an external path for catalyst delivery. However, a high catalyst-to-carbon ratio led to iron agglomeration, reducing efficiency, while insufficient carbon at critical temperatures limited CNT growth [20]. Osorio et al. [21] changed their single-stage CVD setup by adding an extra quartz tube. The crucible was placed partially inside the furnace, where ceramic nanopowders (alumina, silica, and zirconia) were positioned, while the ferrocene (used as the catalyst and C source) was kept outside reactor chamber. The low yield with poor quality

CNTs could be attributed to limited C supply. In another study, the FC-CVD was modified with inlet ports to the quartz tube to minimize side reactions from precursor chemicals. However, the resulting CNTs were randomly oriented with a low yield [22].

Lee et al. [18] were the first to highlight the significance of the distance between the precursor chemical source and the CVD reactor zone in CNT product quality with improved yield via the ferrocene route. When precursor chemicals in the ferrocene method were injected directly at the inlet of the tube, iron particulates approximately 15 nm in size predominated, collecting on the surface of a rotating rod [18]. However, further research is needed to determine the optimal catalyst size, CVD configuration, and how it could be adjusted by varying the distance between the precursor source and the reactor zone.

However, the versatility of single-stage CVD systems for CNT production using the metallocene route is often overlooked. Unlike multi-stage CVD setups, single-stage systems allow for the direct introduction of precursor chemicals into the reaction zone by positioning them near the tube inlet, using pre-mixed substrates with precise ratios. The high thermal conductivity of the tube material effectively controls the temperature gradient in the inlet zone, ensuring it is sufficient to vaporize the chemical sources required for CNT production. The vaporized precursor mixes smoothly with the continuous carrier gas flow, ensuring a uniform feed into the reaction zone. This setup allows for fine-tuning of the pathway from the source to the CVD reaction zone, optimizing conditions for high-yield CNT production. Utilizing the reaction zone as the substrate facilitates a narrow diameter of catalyst deposition. The high-density active catalyst area is vital for facilitating increased carbon deposition, which is crucial for attaining a high yield of VACNTs.

The activity and selectivity of supported catalysts for growth CNTs are significantly influenced by several key factors, including the type and structure of the support, the preparation method, and the loading of active sites, such as the percentage of iron. These elements play a crucial role in determining the catalysts' redox properties and particle size [23]. The " metallocene route" in CVD production of VACNTs uses various substrates like silicon [24, 25], copper [26], and alumina ceramics [21, 27, 28], each requiring distinct configurations. Silicon and copper need a specific crystallographic orientation [29] or buffer layer [30, 31] to enhance VACNT growth, while alumina ceramics, with their stronger interaction and high surface area, prevent metal nanoparticle aggregation and facilitate VACNT formation [28, 32]. Alumina's chemical inertness also minimizes iron diffusion. Alumina is commonly used in the construction material of CVD components, such as tubes, due to its stability under heat. In previous studies, most investigations

were conducted on separate flat surfaces and ignored the role of CVD substrates. Stephanie et al. highlighted several limitations of CNT growth on concave surfaces and identified improved processes for growing CNTs on the inner walls of full tubing [33]. Heated coils in the furnace transfer heat directly to the inner wall substrate surface, effectively deposition of catalyst and carbon source. This approach ensures that the substrate uniformly reaches the target temperature, creating a stable thermal environment crucial for the consistent growth of VACNTs. The single-step CVD processing offers significant potential for automation from the initial to the final stage product without multiple steps such as precursor loading, substrate coating, reaction monitoring, and product collection without any modification.

We optimized a single-stage FC-CVD system for VACNT production on alumina ceramic surfaces in the reaction zone using the ferrocene (catalyst) and camphor (carbon source) route. The VACNTs produced were characterized using scanning and transmission microscopy, infrared and Raman spectroscopy, thermogravimetric analysis and X-ray photon spectroscopy. Investigations on CNT growth mechanisms show that environmental factors significantly impact growth, with varying theories on nanoparticle roles contributing to ongoing research. The growth mechanism and behavior of Fe particles were analyzed through a detailed evaluation of the characterization results, and VACNT hydrophobicity was assessed through contact angle measurements. When CNTs are synthesized via the ferrocene route, additional functionalization is unnecessary making them widely studied as promising adsorbents for heavy metals. This synthesis mechanism shows significant potential for cost-effective, large-scale production of VACNTs via the metallocene route in a simple CVD setup under controlled conditions.

Experimental

Materials

Analytical grade ferrocene, H_2SO_4, H_2O_2, $K_2Cr_2O_7$, $NaNO_3$, methanol, and acetone were received from Sigma Aldrich (USA). Camphor tablets were also obtained from McSons Organics (Pvt) Ltd, Sri Lanka. Non-thermally oxidized- Si (100) plates were donated by Novena Tec (Sri Lanka). Cu (111) was purchased from Lanka Brass (Pvt) Ltd, Sri Lanka.

VACNTs synthesis

A single-zone CVD furnace (tube: 75 mm ID and 1000 mm length, made of alumina ceramics) was used to synthesize VACNTs (KJ-11400, Kejia, PR China). The zonation of the temperatures in various segments of the CVD reactor is shown in Fig. 1. Nitrogen (99.999%, purity) was used as the carrier. Within the CVD the gas flow rate was controlled at ± 1.0 sccm resolution. The middle zone of the heating coil generates a constant temperature zone (Zone B) of 300 mm, maintained at 850 ± 1 °C within the range of 35 to 65 cm [33]. A temperature gradient naturally forms at the tube ends (Zones A
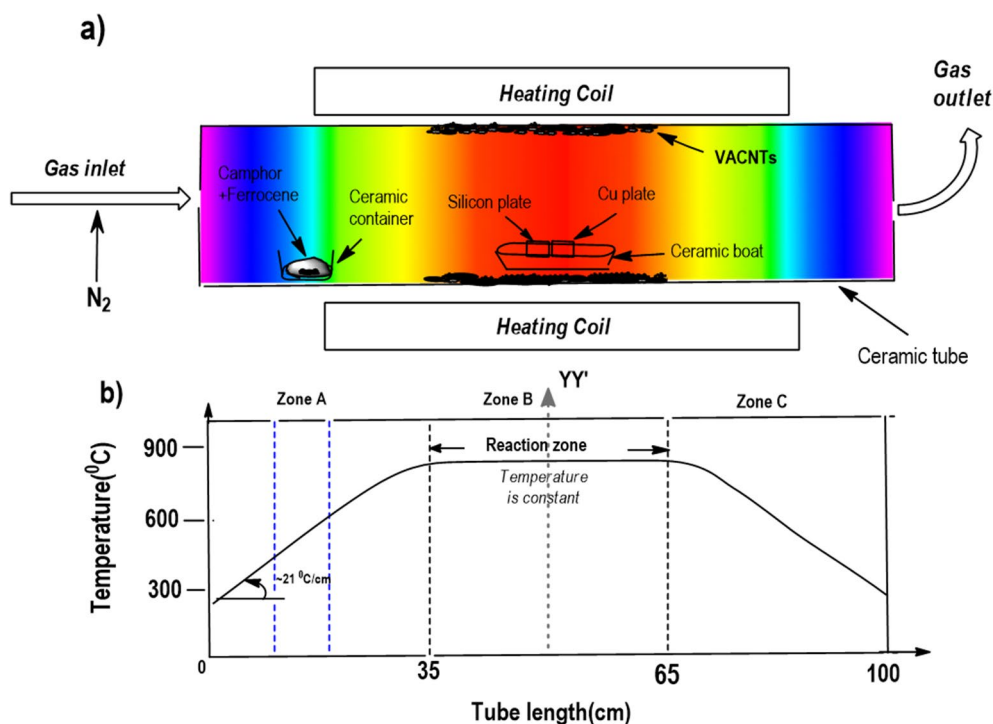

Fig. 1 A schematic diagram of the single-zone furnace along with the synthesis of collector materials and **b**) thermal profile along the axis of CVD

and C, Fig. 1-b). Therefore, the region between 35 cm and 65 cm is considered optimal for CNT growth [34]. The nitrogen carrier gas flow was maintained at 400 cm³STP/min (sccm) from the initial step to ensure laminar flow along the reactor's coaxial axis [35]. Residence time, controlled by adjusting the flow rate, plays a crucial role in ensuring complete precursor pyrolysis and effective interaction with catalyst sites, promoting uniform CNT growth [36]. Longer residence times (~52s) facilitate effective interaction between reactive species and the more active catalyst sites on the alumina surface, resulting in uniform and high-quality CNT deposition.

Producing VACNTs using the standard CVD procedure with a camphor/ferrocene system encountered issues due to lab-specific conditions. In our setup, gas-phase vapors from the camphor and ferrocene mixture condensed inside the connecting copper tube (from the round-bottom flask to the CVD furnace) due to temperature differentials between the inner and outer tube surfaces (Fig. 1-S). Insulating the tube did not resolve the issue. This condensation prevented the vapors from effectively reaching the furnace, resulting in a significant amount of unreacted chemicals remaining in the flask and, consequently, a reduced CNT yield. Given our current limitation to a single-stage CVD setup, we positioned the chemical sources within the inner tube. We adapted a simplified, reliable method to overcome these condensation and vapor flow challenges. This adjustment is the primary motivation for transitioning to a single-stage floating catalyst CVD approach.

A mixture of camphor and ferrocene in a ratio of 20:1 was placed near the left end (15 cm) of the ceramic tube. Then, the alumina ceramic boat was placed on the alumina ceramic tube in the middle zone (Fig. 2-S). In a typical experiment, the furnace was heated to the desired temperature (850 °C) at a heating rate of 10 °C.min^{-1} while under atmospheric pressure, and N$_2$ (400 sccm) was purged into the tube. We predominantly used an alumina ceramic substrate to grow CNTs, however we also tried Si (100) and Cu substrates. A comparison of the materials thus resulted is given in support documentation. In that case, the Cu/ Si substrates were kept at the center of the tube as shown in Fig. 1-a.

The formation of VACNTs started on the surfaces at 850 °C and continued for 1 h with a steady flow rate of high purity N$_2$ at 400 sccm. (Fig. 3-S). Further, the N$_2$ feed was maintained until the reactor achieved ambient temperature. The CNT products on the silicon wafer, copper plate, ceramic boat, and inner wall of the tube were collected, individually.

The ferrocene and camphor were pre-mixed in a ceramic container to ensure homogeneity and then placed in the CVD reactor's pre-heat zone (Zone A). This zone has a temperature gradient of 21 °C/cm and is situated 0 to 35 cm from the reactor zone (Zone B). The mixture was maintained under a N$_2$ carrier flow. The temperature profile inside the CVD reactor composed of ferrocene, camphor, and their degradation products under the N$_2$ flux stabilized within 90 min (Fig. 3-S). The wettability of the substrates thus produced was determined by contact angle measurement using ImageJ software [37].

VACNTs characterization

The carbon nanotubes (CNTs) thus collected from the various substrates were examined by X-ray diffraction spectrometer (XRD) at a scanning speed of 4° min$^{-1,}$ and 2θ ranges from 10° to 60° (Rigaku Ultima IV Cu-Kα radiation, λ = 0.154056 nm, Japan). Transmission electron microscopy (TEM, JEM-1400flash, Japan) and scanning electron microscopy (SEM, ZEISS EVO 40 SE detector, Germany) measurements were used to analyze the morphology and microstructures of the VACNTs. The materials' functional groups and near-surface elemental composition were investigated by X-ray photoelectron spectroscopy (ESCALAB250Xi Thermo, USA). A Raman spectrometer (Thermo Nicolet DXR, USA, λ = 780 nm) was used to obtain the spectrums of the substrates. The FTIR spectra were recorded in transmission mode to characterize surface sites with an IR spectrometer equipped with a DTGS detector (model iS50 Thermo Scientific, USA). Thermal analysis of the sample was also performed using DSC-TGA equipment (TA SDT 650).

Chromium(VI) adsorption

The Cr(VI) removal by 5.00 ± 0.01 g/L CNTs was determined using a simulated water sample with the composition: pH 5.00 ± 0.01, 2. mg/L Cr(VI). Chromium adsorption isotherm for CNTs was constructed at 298 K using the following initial conditions; 1.0–10.0 mg/L, CNTs 5.00 ± 0.01 g/L, pH 5.0 ± 0.01. The 20 mL of chromium and CNTs suspensions were equilibrated in 50 mL centrifuge tubes using an end-to-end shaker (MS-RD-Pro Rotor, HINO- TEK China). The particulate separation from the solution was carried out using 0.22 μm syringe filters. The chromium was measured by using a UV spectrophotometer (Shimadzu 2450 UV-VIS) at a wavelength of 540 nm. The chromium removal efficiency by CNTs was determined as follows:undefined

$$\text{Chromium removal Efficiency}$$
$$= \frac{[\text{Cr (VI)] initial}- [\text{Cr (VI)] final}}{[\text{Cr (VI)] initial}} \times 100\%$$

The chemical kinetics of chromium adsorption by CNTs was examined using a 500 mL batch reactor containing 2.5 mg/L Cr(VI) and 5 ± 0.01 g/L CNTs at pH 5.20 ± 0.01 in 0.01 M NaNO$_3$ at 298 K. When VACNTs are mixed

with a solution, the bundles break apart into individual CNTs, which are subsequently referred to as CNTs in Sect. 3.5.2.

Result and discussion

Single-stage FC-CVD for VACNTs growth

We initially implemented a CVD system derived from SSCVD that used an external heater to vaporize the camphor (C source) and ferrocene (Fe catalyst). In this process, CNTs were synthesized on the silicon (100) substrate using camphor and ferrocene at 850 °C. The SEM images reveal the morphology of randomly oriented CNTs grown on the silicon substrate, with an average diameter of approximately 80 nm (Fig. 4-S). The low yield of nanotubes resulted in bent structures that grew in random directions, lacking support from neighboring nanotubes. Thus, the bundles of CNTs formed to appear more loosely packed and agglomerate with a "combed yarn" structure. The high-magnification SEM image shows denser agglomerates with a "bird's nest" structure (Fig. 4. b-S). The non-uniform evaporation of ferrocene and camphor during the synthesis process led to less dense CNTs with low carbon content, poor alignment, and random orientation of the nanotubes. Since sufficient vapors did not reach the tube and a surplus of mixed chemicals remained in the flask after the process, the formation of VACNTs could not be observed.

To mitigate this challenge, we employed a single-stage floating catalyst chemical vapor deposition (SS-FCCVD) system using ferrocene and camphor without an external heater and an explicit growth substrate for VACNTs production. In contrast to SS-FCCVD, double or multi-stage (DS) FCCVD systems are commonly employed to fabricate CNT variants. DS-FCCVD allows independent temperature control for each oven [38], yet rapid temperature gradients especially during substrate transfer from low to high-temperature ovens may induce amorphous material formation alongside the desired product. We posit that SS-FCCVD exhibits higher temperature gradient heterogeneity than DS-FCCVD. Additionally, SS-FCCVD systems offer greater customization to specific requirements compared to their DS counterparts (Table 1-S).

Further, SS-FCCVD offers significant advantages, one of the key benefits is the simplified setup, which requires fewer resources and operational steps. Unlike double-stage systems, SS-FCCVD eliminates the need for additional setup and complex catalyst pre-deposition steps. SS-FCCVD also ensures consistent temperature and gas flow conditions, optimizing the growth environment for VACNTs and resulting in faster growth rates and enhanced uniformity. The direct introduction of precursor chemicals into the reaction zone allows for better catalyst efficiency and more uniform distribution, leading to higher-quality CNTs with consistent alignment and diameter. Moreover, SS-FCCVD reduces energy consumption by maintaining a more uniform thermal profile and optimizing the use of chemical sources, which contrasts with double-stage CVD that requires more energy to control multiple reaction zones. Additionally, the single-stage process allows for direct CNT growth onto substrates, eliminating the need for pre-deposited catalysts and making it a more scalable and efficient method for large-area production.

In SS-FCCVD, distinct zones such pyrosis, nucleation and reaction zones play a crucial role in ensuring the efficient catalyst activation, carbon feedstock decomposition, and VACNTs formation, respectively (Fig. 2). Both the pyrosis and nucleation zones are interpreted in Fig. 1 as Zone A. The shorter flow paths for catalyst transfer to the reactor zone (Zone B) result in more efficient reactant throughput. Typically, the particle diameter is increased along the CVD tube due to the collision and coalescence [15]. Controlling the nucleation zone in a CVD process reduces the size of Fe particle, a shorter distance minimizes the time particles have to aggregate, leading to finer particles with less opportunity for coalescence (Fig. 2). It is crucial, however, to maintain steady-state temperature in zones for the success of the method (Fig. 1. a).

Both ferrocene and camphor possess comparable boiling and melting points (ferrocene melting point, MP, 174 ^{0}C, boiling point, BP, 249 ^{0}C; camphor MP, 180 ^{0}C, BP, 204 ^{0}C), therefore they can form a homogeneous gaseous mixture at camphor /ferrocene ratio 20:1 around 850 ^{0}C. Due to the difference in heat of vaporization (ΔH_v) (ferrocene, ΔH_v 74±3 kJ/mol; camphor ΔH_v 51.9 ± 0.8 kJ/mol) and camphor/ferrocene ratio 20:1, camphor is dominant in the gaseous phase [39]. To optimize the precursor placement along the CVD tube effectively, it is crucial to understand the thermal decomposition behavior of ferrocene, which predominantly occurs at temperatures exceeding 500 °C, resulting in the formation of Fe atoms [40]. By positioning the precursor 15 cm from the inlet (pyrolysis zone), within the operational temperature range of 400 °C to 600 °C, the precursor is subjected to a sufficiently high-temperature gas flow that enhances its decomposition and subsequent transition to catalyst particles (Fig. 2). This strategic placement not only ensures effective exposure to optimal thermal conditions but also facilitates the formation of catalyst particles within the narrow size distribution, which is critical for catalytic efficiency [18]. Furthermore, this configuration allows for a dynamic adjustment of precursor positioning based on real-time monitoring of particle characteristics, leading to improved catalytic activity and product quality.

The structural properties of the reaction zone, such as its curvature and area, play a vital role in enhancing the quality and high-density growth of VACNTs. The precise
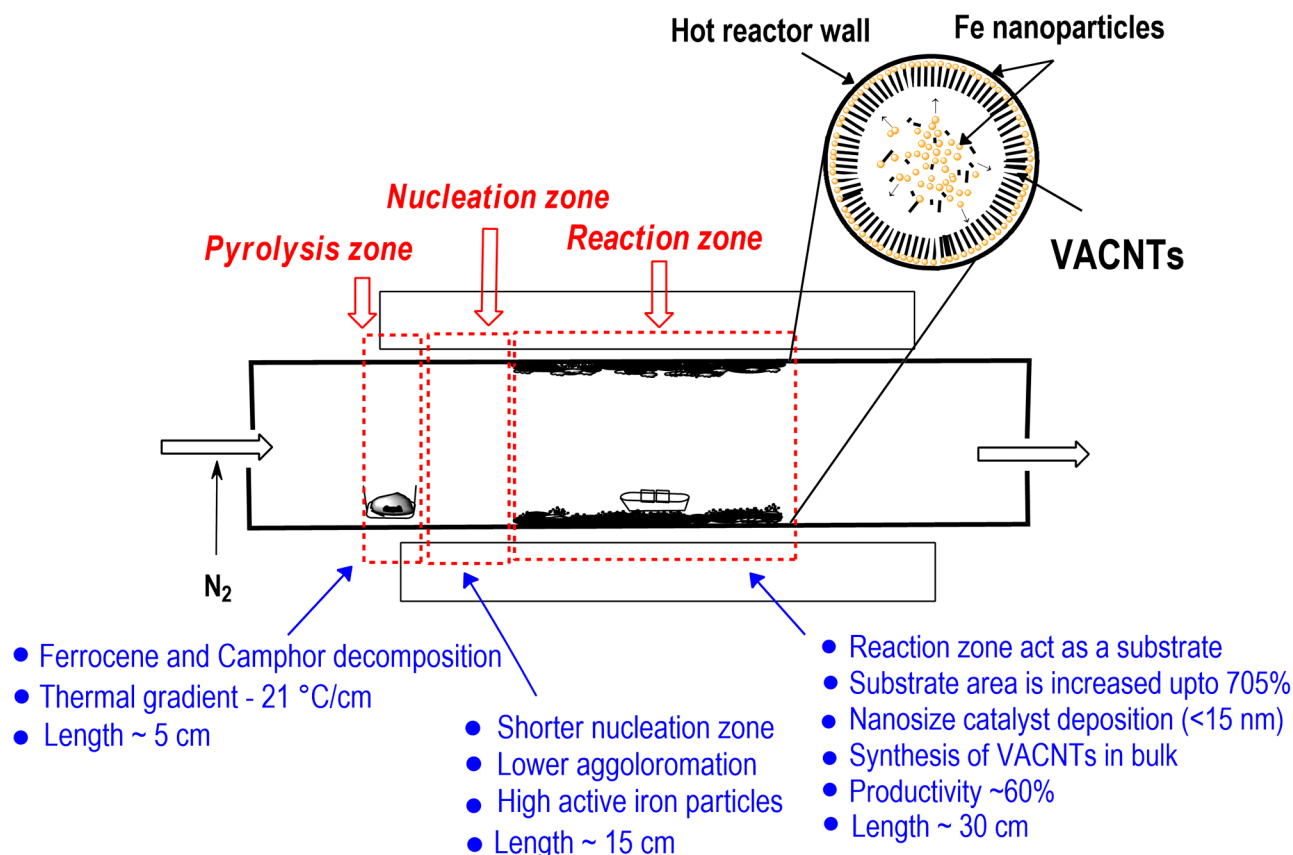
Fig. 2 Schematic of the Single-Stage Floating Catalyst CVD (SS-FCCVD) system for VACNTs synthesis, and illustrating the role of each zone

temperature control within the reaction zone, along with the expanded active substrate area up to 705% (with a diameter of 75 mm and a length of 300 mm), improves the effective deposition of tiny iron particles with high density. (Fig. 2) This enhancement increases the number of active catalyst sites and facilitates the steady production of high-quality VACNTs. As the VACNT forest grew perpendicular to the concave substrate, the decreasing circumference constrained the available space. As a result, the increased circumferential compression caused the CNT ends to press against each other, promoting high-density CNT growth on concave surfaces [33]. However, using the inner walls of the CVD tube as a concave substrate is a notable novelty of this work. Our results indicate that inner wall of alumina ceramic surfaces, unlike silicon (Si) or copper (Cu), can be directly used as substrates for large-scale VACNT production without any modifications.

Alumina ceramics morphology for VACNT growth
The yield and quality of VACNTs are determined by both the composition and morphology of the solid substrate used, as well as the CVD configuration, with both factors being equally important [41] (Table 2-S). Mosallanejad et al. [23] discussed the surface chemical properties

of alumina, noting that the positively charged surface of alumina (the point of zero charge;7 to 9) assistances in minimizing agglomeration by enhancing electrostatic repulsive forces and reducing the size of catalyst clusters. Alumina-supported iron oxide catalysts exhibit stronger interactions between the iron species and the support, leading to more stable configurations and higher coordination environments [42]. In contrast, silica-supported iron oxide formed larger surface particles due to weaker interactions with the support, which influenced the adsorption behavior of molecules such as NO [23]. Microscopy images revealed that the catalyst particles are nearly spherical with a relatively small diameter on alumina surface. Also, iron dispersion on alumina was significantly better compared to silica, as indicated by CO-chemisorption measurements showing a dispersion of 6.2% on alumina versus only 1.95% on silica [23]. (Fig. 3) This higher availability of active sites on the iron surface has also led to higher carbon deposition [43].

Although, surface roughness also plays a pivotal role in suppressing the diffusion and coalescence of catalyst particles, a key factor in facilitating the growth of aligned CNTs. In terms of roughness, commonly used substrates for CNT growth can be graded as follows: Si (atomically smooth, such as polished wafers) < SiO_2 (low roughness,
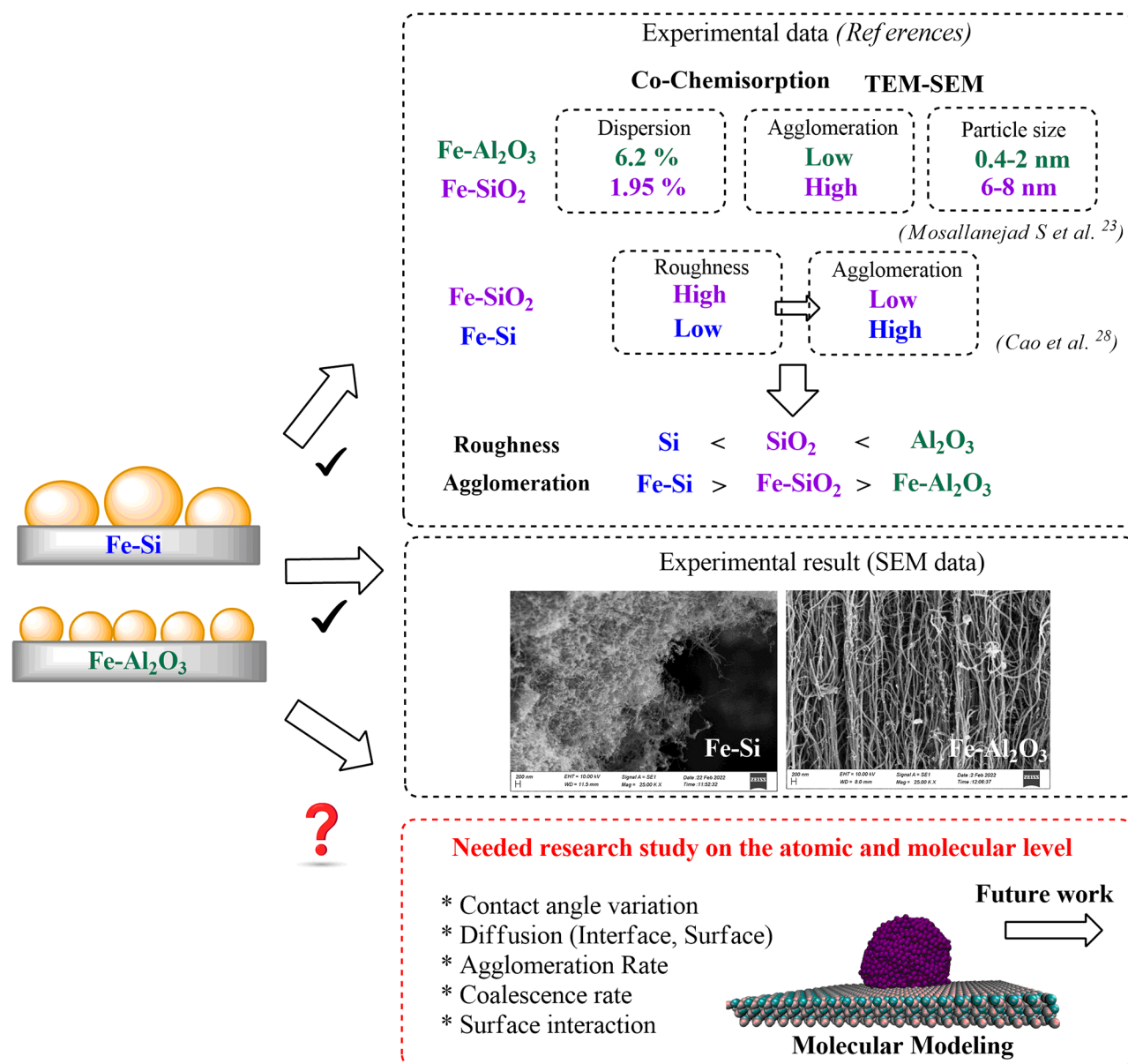
Fig. 3 Surface chemical properties of alumina, SiO_2 and silica surface for Fe particle distribution and growth of different morphology of CNTs

higher than silicon) < Al_2O_3 (typically rough, with surface roughness ranging from 1 to 10 nm). However, Cao et al. observed that while aligned CNTs grew on SiO_2 substrates, both excessively high surface roughness (rough polycrystalline ceramic substrates) [28] and low surface roughness (Silicon (111) plate) [44] resulted in randomly oriented CNTs. Interestingly, breaking a Si (111) wafer creates a rough cross-section, which enhances surface roughness and accelerates the growth of aligned CNTs. Regardless of the oxidation process, the degree of roughness effectively prevents catalyst particle diffusion and unification [44]. Therefore, controlled surface roughness is a critical parameter for achieving aligned CNT architectures. These chemical and physical properties make

Al_2O_3 an ideal substrate for promoting the growth of VACNTs. (Fig. 3)

Table 1 shows the yield of CNT produced on different ceramic substrates by FC-CVD using different C sources in the presence of ferrocene catalysts. However, the precursor mass introduction methods into the synthesis chamber and the configurations of the CVD differ which seem to affect the CNT quality and yield.

The SS-FCCVD method allows to generation of small iron particles in the gas phase before deposition, enhancing control over their final characteristics (Fig. 2). Simultaneously, carbon precursors decompose on these well-dispersed catalytic nano-Fe particles within the non-catalytic Al_2O_3 matrix, promoting the formation of

Table 1 The different morphology of CNTs on different ceramics substrates in the ferrocene catalyst FC-CVD system is shown

C Source	Substrate	CVD system	Growth Rate	Limitation	Source
Melamine	Polycrystalline ceramic wafers	Three stage CVD	1.66 µm/min	Randomly oriented CNTs (60 min)	Cao et al. 2007 [28]
Camphor dissolved in hexane	Ceramics plate	Double stage CVD	30 µm/min	VACNTs L:0.3 mm (10 min)	Braga et al. 2020 [27]
Ferrocene	Ceramic powders (alumina/silica/zirconia)	Single stage (Extra equipment)	(No data)	Randomly oriented CNTs	Osorio et al. 2013 [21]
Camphor	Alumina ceramic boat	Single stage	20 µm/min	VACNTs L: 1.2 mm	This work
Camphor	Alumina ceramic tube	Single stage	16 µm/min	VACNTs L: 1.0 mm	This work

well-aligned CNT arrays. The alignment of CNTs is a result of the "crowding effect" and van der Waals interactions, where each CNT finds support from its neighboring counterparts, contributing to the overall well-aligned structure [45]. In addition to using a solid growth material externally, the surfaces of the reactants' containers such as alumina ceramic tubes or ceramic boats were also utilized as growth substrates. In our process, CNT growth was observed on alumina ceramic segments of the SS-FCCVD, distinguishing it from other studies. In contrast, CNTs tend to grow in random directions on larger iron particles deposited on the smooth silicon surface, consistent with the findings of Cao et al. (Fig. 5-S).

Inside the inner walls of the ceramic tubes (inner diameter 7.5 cm and 100 cm long), CNT tubes of 1.0 mm and 50 nm diameter are grown orderly. Due to a flow perpendicular to the face surface of the ceramic boat, VACNTs grow about 1.2 mm with a dimension of 60 nm. Compared to these results our method resulted FC-CVD with the highest CNT length so far reported (e.g., 1.2 mm on the boat with a growth rate of 20 µm/min). This experiment produced approximately 10 g of the VACNTs with low impurities, employing 17 g of camphor as the carbon feedstock (productivity ~ 60%). A brittle carpet of amorphous and graphitic carbon structures was observed on a copper substrate (Fig. 6-S). Research indicates that the addition of catalyst supply layers is critical for the successful deposition of CNTs on copper plates [46]. Bare copper, without a barrier layer, is generally incapable of supporting nanotube growth. This limitation may stem from the atomic diffusion of the catalyst into the copper substrate, leading to insufficient catalyst availability for CNT formation.

VACNTs characterization

SEM and TEM images of the side and surface of a VACNTs array are shown in Fig. 4. When initiating CNT formation, the growth of the tube tends to continue in the same direction and is reinforced by the presence of surrounding nanotubes (Fig. 4. a). In both occasions, the CNTs are well aligned and smooth with consistent hollow structures and are self-assembled into bundle-like structures. Due to van der Waals interactions, the nanotubes are orderly packed.

Additionally, the TEM images reveal instances of bridged tube walls filled with carbon-encapsulated Fe particles in the growing process. (Fig. 4. b, c, and d). In the latter case, ~ 5 graphitic layers' surround Fe moieties (Fig. 4.d). As in Fig. 7-S, the Fe particulates possess cylindrical and spherical shapes (Dark nanoparticles). Additionally, the inner channels of multi wall CNTs are typically hollow or mostly empty. When these Fe moieties are covered with graphitic structures, their catalytic activity seems reduced and protects the metal core from oxidization or other reactions [10]. Further, the C-coated Fe particulates are heavier than their bare analogs. Therefore, bare Fe seems to cluster in the gas phase whereas graphitic structures coated Fe tend to deposit on the growth surface. The surface-adhered graphitic structures on Fe may loosen to nucleate CNT. But, these findings are in contrast with the previous studies [10]. Based on our characterization results, it was concluded that carbon-encapsulated particles in the gas phase can directly attach to both the inner and outer surfaces of the CNTs. When deposited on the inner surface, additional carbon layers grow, covering these encapsulated particles. (Fig. 4. c)

The crystallographic features of VACNTs can be confirmed with TEM, XRD, and Raman data. The distinct XRD peaks at $2\theta = 26.2°$ (d = 3.40 Å) and $2\theta = 44.2°$ (d = 2.05 Å) correspond to the graphitic structures can be assigned as to (002) and (100) planes, respectively. As shown in TEM and XRD data, the VACNT has a layer distance of ~0.35 nm (Fig. 5. a). The highest crystal dimensions of 6.44 nm and d_{002} of VACNTs grown on the inner wall were estimated according to the Debye-Scherrer method and Bragg's equation. As shown by narrow peaks, well-crystalline CNT substrates were obtained [47] (Fig. 5. a). These results reveal that the crystalline graphitic sheets are parallel to the tube axis and well-aligned. Thus, the inner diameter of CNTs is around 10 nm and consists of ~15 layers of concentric graphitic sheets. (Fig. 5).

A detailed analysis of the 2θ range from 35° to 55° reveals several distinct peaks corresponding to various forms of iron. (Fig. 5. a) However, the lower intensity peaks at the XRD spectrum for iron species confirm that
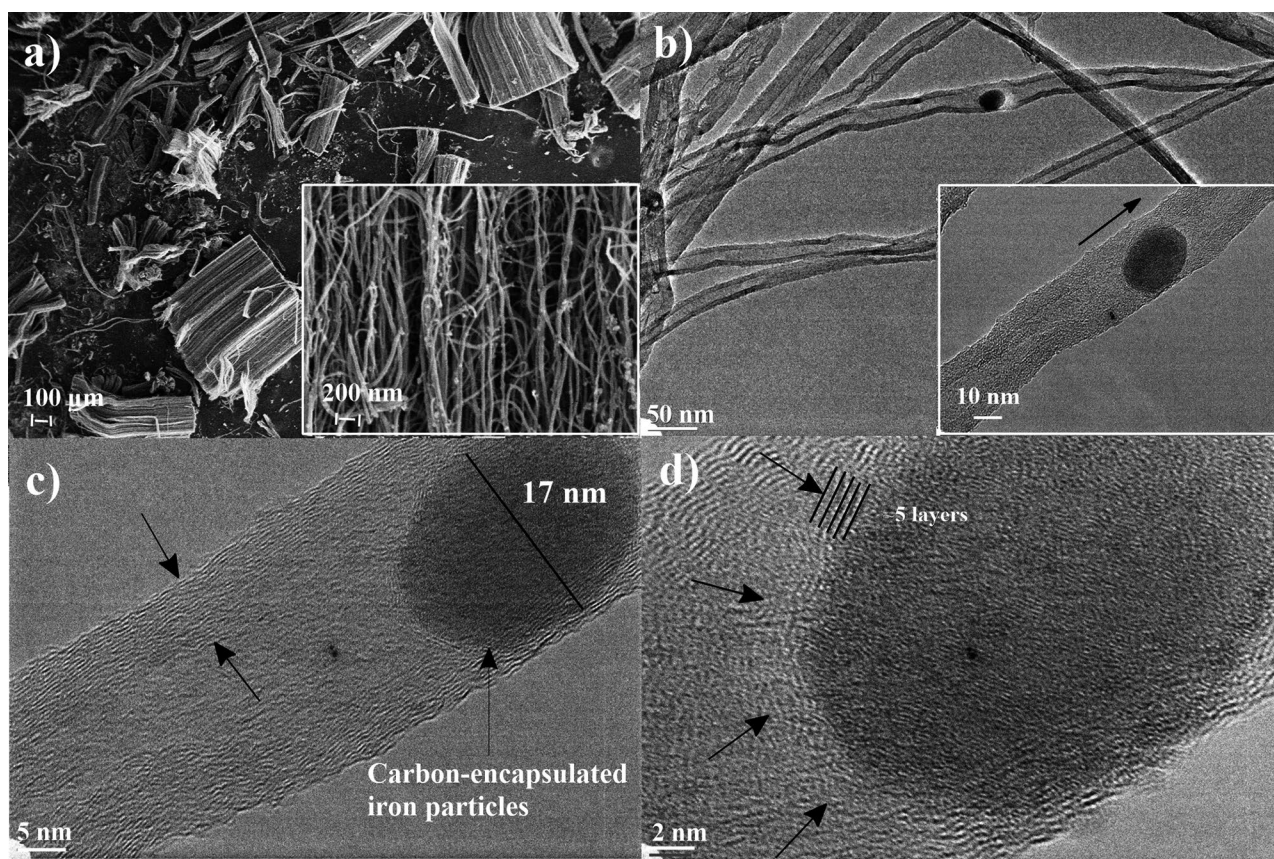
Fig. 4 Images of VACNTs on the ceramic surface. (**a**) SEM images of oriented long VACNTs array bundles 1 mm in length. Inset is the enlarged image. (**b**) TEM images of individual straight VACNTs with the iron nanoparticle. The direction of growing paths slightly changes due to the iron particles. (**c**) An individual nanotube with graphitic carbon layers (~5 layers) and a diameter of the iron particle is ~17 nm in the nanotube. The inner diameter of CNTs is around 10 nm and **d**) TEM image of a carbon-encapsulated iron core with ~15 graphitic layers in the nanotube (VACNT can also be designated as VA-MWCNT)

these CNTs contain a lower concentration of iron particles compared to those produced by other methods, even when ferrocene is used as the catalyst in FC-CVD [48]. At elevated temperatures ranging from 700 to 900 °C, iron readily reacts with carbon to produce iron carbide (Fe_3C). This process is driven by the high carbon availability and the thermal conditions in the reaction zone. The presence of an XRD peak at $2\theta = 37.9°$ indicates the formation of Fe_3C. This Fe_3C phase frequently serves as a catalyst, facilitating the ongoing decomposition of carbon precursors, which in turn promotes the growth of CNTs and the encapsulation of iron particles. The peak at $2\theta = 45.2°$ confirms the presence of bare metallic iron (zero-valent iron) on the CNTs. Additionally, the peaks at $2\theta = 35.6°$ and $53.5°$ indicate the presence of iron oxide, primarily formed due to oxygen exposure from release from camphor and the ambient air at room temperature [49].

The small presence of certain defects, such as kinks, twists, or breaks can also be observed as distortions of the lattice pattern. The graphitic G mode (tangential mode, E2g band) and the second-order double-resonance 2D peak, arising from the double-resonance mechanism, are observed at 1581 cm⁻¹ and 2651 cm⁻¹, respectively. The disordered structure-related D peak (breathing mode, A1g band) is observed at 1315 cm⁻¹, corresponding to CVD-synthesized VACNTs [50]. Upon further analysis of our Raman spectra, a hematite peak was observed in the lower range (200–800 cm⁻¹).(Fig. 5.b) In geological sample analysis, the mineral fingerprint region (200–800 cm⁻¹) is typically used to identify metal oxides and other inorganic compounds, while the carbon first-order region (800–1800 cm⁻¹) is used to study carbon-based materials [51].The hematite-associated peaks observed in our analysis include those at ~ 185 cm⁻¹ (Fe_2O_3) [52], ~ 231 cm⁻¹ (α-Fe_2O_3) [53], ~ 288 cm⁻¹ (associated with nanosizing effects on hematite lattice and magnon modes) [54], ~ 392 cm⁻¹ (α-FeOOH) [55], ~ 494 cm⁻¹ and ~ 609 cm⁻¹ (α-Fe_2O_3) [53], and ~ 720 cm⁻¹ (γ-Fe_2O_3) [55] (Fig. 5.b).

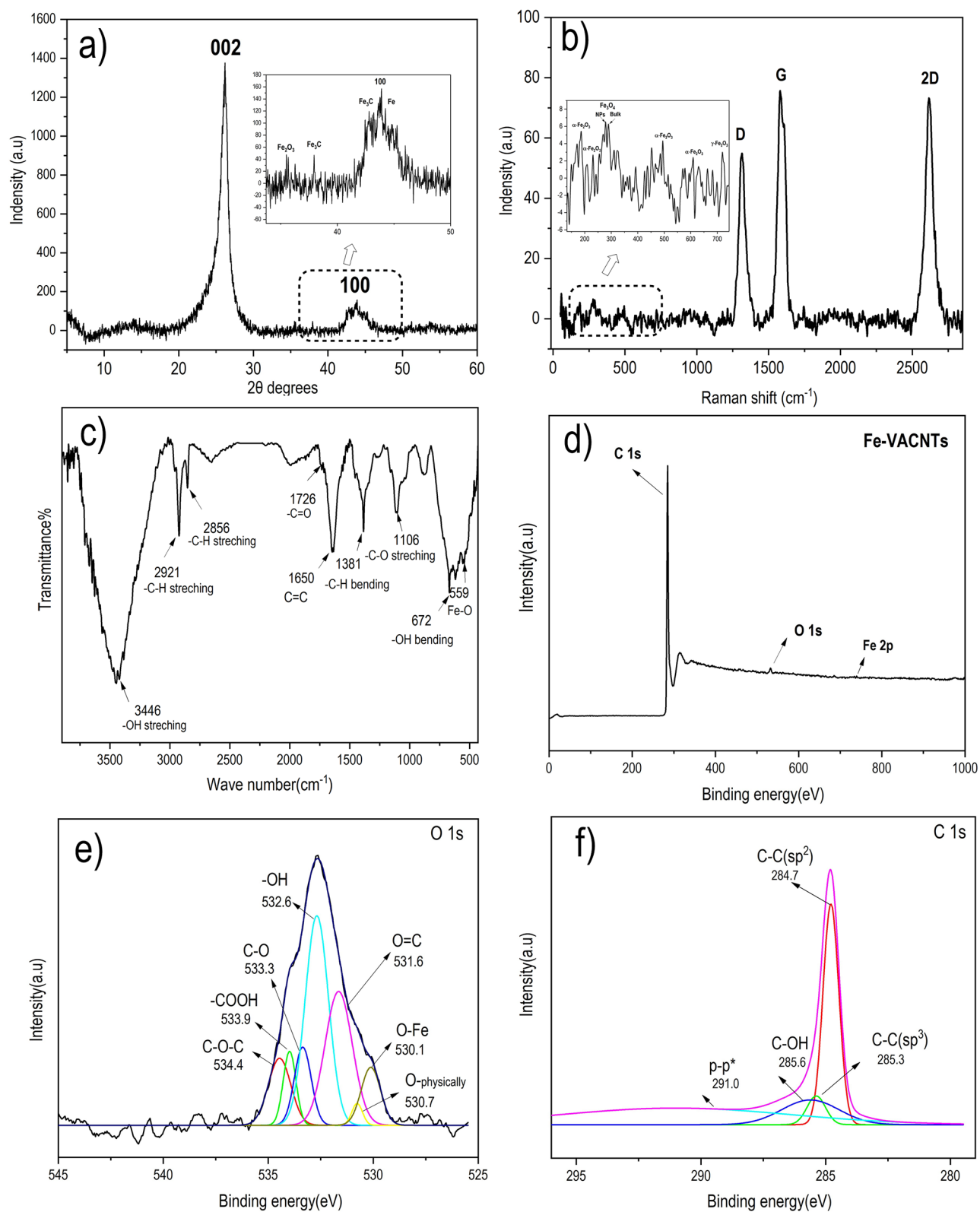Typically, both the relative magnitudes of (I_D/I_G) and (I_D/I_{2D}) ratios can be used to assess the degree

Fig. 5 (**a**) XRD pattern (**b**) Raman pattern (**c**) FTIR spectra (**d**) XPS scanning spectrum (**e**) and XPS high-resolution survey scans of: (**f**) C1s spectrum; and (**g**) O1s spectrum of VACNTs on the on inner wall of the furnace

of defect or disorder of the nanotubes. The (I_D/I_G) and (I_D/I_{2D}) values of the VACNTs are 0.81 and 0.83 respectively. The high-intensity 2D band indicates highly organized nano graphite with few graphene sheets or low defect density 3D structures [56]. However, these defects can be functionalized in the presence of adventitious O_2 resulting in hydrophilic groups as -C-OH, -C=O, and -COOH [57, 58]. Notably, the hematite peak appears within the 1315–1350 cm⁻¹ range, which overlaps with the carbon D-band. Even Raman spectrometer vendors have occasionally misidentified hematite as carbon. This overlap is attributed to the odd symmetry IR-active phonon of hematite, which can easily be misidentified as the D-band of carbon [50]. This spectral overlap complicates accurate phase identification, especially when iron oxides are present with carbonaceous materials, potentially leading to the erroneous conclusion of a higher defect density in carbon structures.

FTIR and XPS spectrums further confirm the presence of functional groups in VACNTs (Fig. 5). The bands at 3446 cm⁻¹, 1726 cm⁻¹, and 1650 cm⁻¹ can be assigned to symmetrical stretching vibration mode of O-H groups [59], stretching of carboxyl group C=O [60] and carbon-carbon double bond [61], respectively. Thus, the peaks at 2941, 2856 cm⁻¹, and 1381 cm⁻¹ were a result of C-H bonds [62]. The FTIR bands at 1106 cm⁻¹ and 672 cm⁻¹ are due to C-O-C carbonyl group [63] and–OH bending. The band at 550 cm⁻¹, attributed to the Fe-O stretching vibration, also confirms the formation of iron particles on CNTs, as evidenced by FTIR data [64].

The XPS survey spectrum shows characteristic bands appear at C1s (284.8 eV), O1s (532.6 eV), and Fe 2p (707.5 eV). The O1s band deconvoluted into 530.1 eV, 530.7 eV, 531.6 eV, 532.6 eV, 533.3 eV, 533.9 eV, and 534.4 eV peaks (Fig. 5.e) [56]. The spectrum of physically absorbed O1 (O-VACNT) shows some intensity at the corresponding Binding energy (BE) of O1 (530.7 eV) [65]. The peaks 531.6 eV, 532.6 eV, 533.3 eV, 534.4 eV, and 533.9 eV show the presence of the C=O, O-H, and C-O, C-O-C, and -COOH functional groups on VACNT, respectively [66, 67]. As in Fig. 5.f, the C1s deconvoluted into peaks correspond to sp^2 C (284.7 eV), C-C (285.3 eV), C-OH (285.6 eV), and π-π^* interactions (291.0 eV). With a continuous supply of ferrocene, Fe^0 particles accumulate on the outer walls of VACNTs following growth. These iron particles can eventually oxidize into Fe_2O_3 when exposed to air. The peak at BE (530.1 eV) corresponds to oxygen-metal (O–Fe) bonds (Fig. 5.d) [68]. Detecting Fe-C bonds in XPS is challenging due to overlapping peaks, surface sensitivity, low bond concentration, and the less polar nature of Fe-C bonds, which result in weak or indistinguishable signals. As a result, direct observation of Fe-C bonding via XPS is often difficult.

The overall characterization results showed that different key reactions of ferrocene occur at high temperature in a SS-FCCVD system. Decomposition of Ferrocene: $Fe(C_5H_5)_2 \rightarrow Fe^0 + C_5H_5 + H_2$.

High-Temperature Reactions: $Fe + C \rightarrow Fe_3C$ (iron carbide).
$Fe + O_2 \rightarrow Fe_2O_3$ (iron oxide).
Encapsulation: Fe or $Fe_3C + C \rightarrow$ Carbon-encapsulated Fe or Fe_3C.

As iron is released from ferrocene, Fe particles rapidly flow through the CVD tube and quickly enter the reaction zone. In the high-temperature zone, these Fe particles react with carbon to form Fe_3C and with oxygen to form Fe_2O_3. In a controlled SS-FCCVD environment, oxygen levels are carefully kept low to prevent significant oxidation.

TEM-EDX mapping analysis of the synthesized CNTs (Fig. 6) revealed the random deposition of low iron particles and oxygen concentrations along the CNTs. Specifically, in the regions of carbon-encapsulated Fe and the inner core of Fe (circular areas 1, 2, and 3 in Fig. 6A), the low oxygen content indicates minimal oxidation. Once deposited on the substrate or present in the gas phase, Fe_3C or Fe^0 particles promote the breakdown of carbon sources, leading to the continuous deposition of carbon and the formation of CNTs or carbon-encapsulated iron. Over time potentially encapsulating the Fe_3C core is deposited on both the inner and outer surfaces. This process is confirmed by the TEM and TGA analysis shown in Figs. 6A and 7. Despite the presence of carbon-encapsulated Fe or randomly distributed atoms along the tube, they do not seem to contribute to CNT growth or the formation of amorphous carbon.

The thermogravimetric behavior of VACNTs was investigated under oxidative conditions by heating the samples to 1000 °C at a rate of 10 °C/min in air (Fig. 7). The TGA curves revealed two distinct weight loss regimes, accompanied by residual metal oxide formation. An initial minor mass loss (~1.301%) was observed between 100-450 °C, attributed to the decomposition of oxygenated functional groups (e.g., carboxyl, hydroxyl) and lower level of amorphous carbon [69, 70]. CNTs containing iron exhibited significantly reduced thermal stability, with oxidation starting at 454 °C, whereas pure CNTs began to degrade at approximately 550 °C [71]. This destabilization is likely due to the catalytic role of iron oxide nanoparticles, which enhance localized heat transfer and accelerate carbon oxidation [70]. After combustion of CNT walls exposed to air (450–634 °C), followed by the degradation of carbon-encapsulated carbon structures (553–650 °C). The oxidation of residual iron nanoparticles from carbon-encapsulated carbon
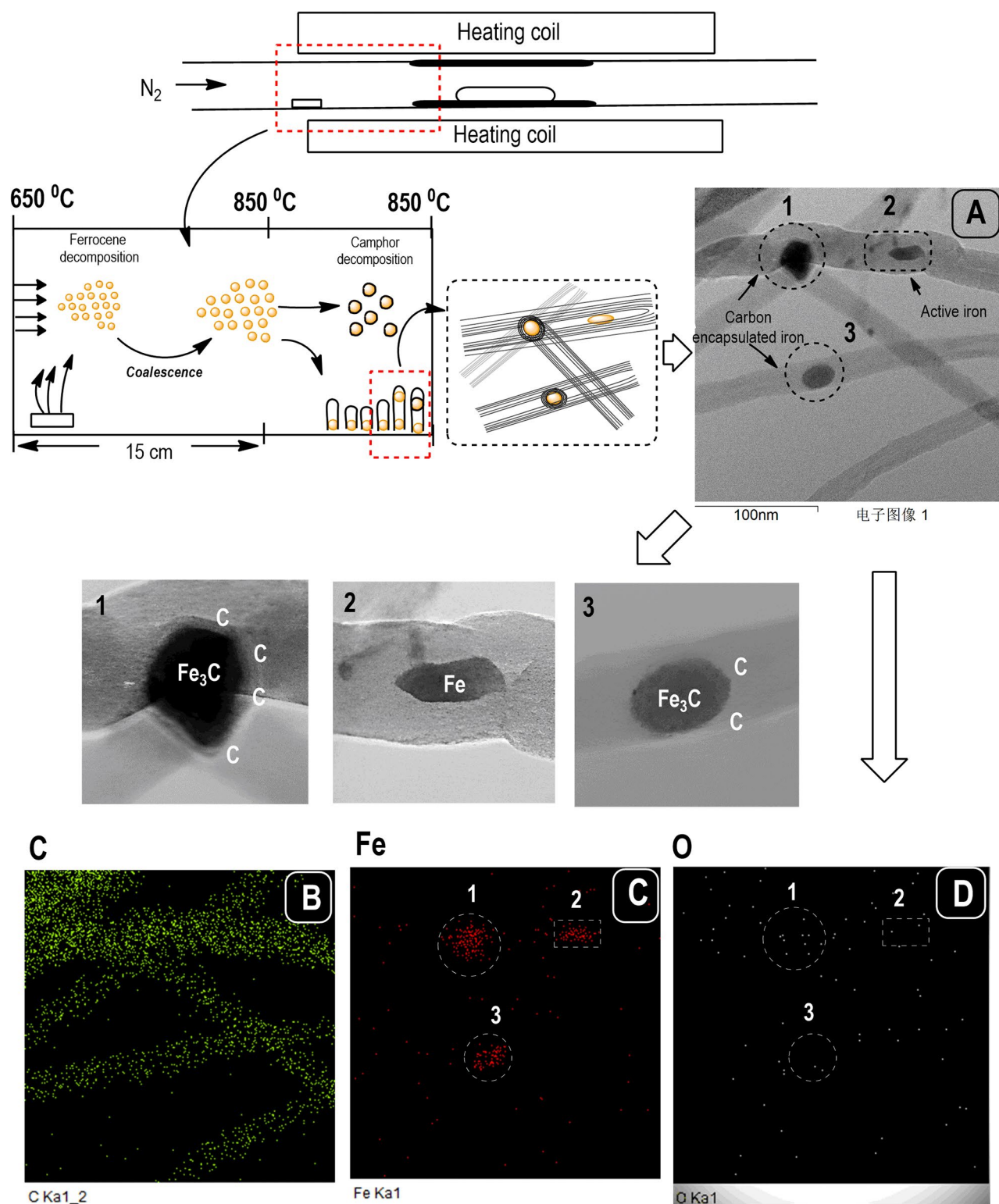
Fig. 6 (**A**) TEM images and (**B**) Carbon, (**C**) Iron and (**D**) Oxygen energy-dispersive X-ray spectroscopy (EDX) spectrum of VACNTs

structures (Fe or Fe_3C) to Fe_2O_3/Fe_3O_4 is demonstrated by the overlap of degradation stages around 600 °C [71]. The temperature fluctuations highlighted that the dynamic interplay of adsorption energy and oxidation kinetics, showcasing the transition from metallic iron or iron carbide to iron oxides as the dominant phase. The weight loss % after 700 °C suggested that the completion loss of carbon leaving only metal oxides. The low residual mass
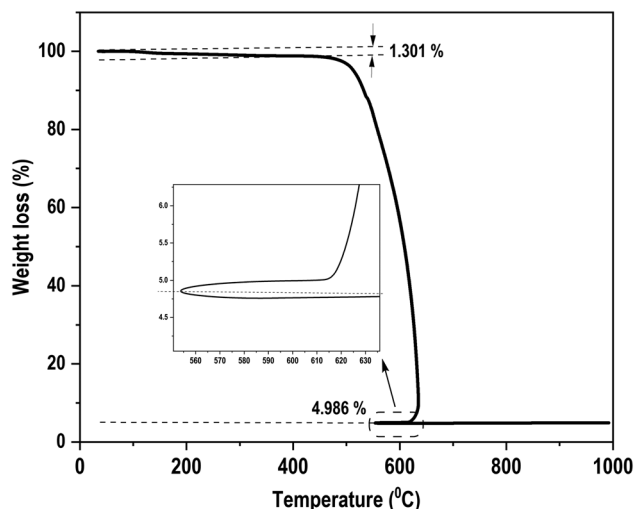
Fig. 7 TGA thermograms of VACNTs sample

of 4.986% was observed, corresponding to iron nanoparticles embedded within the VACNT matrix, confirming a high carbon purity of approximately 95% for the synthesized VACNTs [71]. These results align with the high-quality graphitic structure observed in TEM and Raman analyses, as well as the data presented in Figs. 4 and 5.b.

Growth mechanism of VACNTs

In SS-FCCVD, with a short 20 cm distance between pyrolysis and reaction zones(nucleation zone), high Fe vapor density enriches the reaction zone with small Fe particulates [72, 73]. Fe atoms nucleate into clusters (4–18 nm) in the gas phase [10], and carbon encapsulation occurs when reaching ~10 nm. Larger Fe_3C clusters (>17 nm) impede carbon encapsulation, influenced by system conditions [10] (Fig. 4. b). In the reactor zone, catalyst particles densely intercalate in the range of 20 to 35 nm, settling uniformly on the alumina surface and different collectors. Low laminar flow velocity near internal surfaces prolongs residence times, enhancing iron vapor condensation and forming clusters on the reactor wall. Alumina ceramics act as heterogeneous sites, lowering agglomeration, and promoting CNT formation [74]. Beyond the reaction zone (zone C), decreasing temperature halts Fe evaporation, maintaining constant mass density in the vapor phase, leading to reduced CNT growth in region C. At 850 ^{0}C, camphor predominantly degrades into benzene, with trace amounts of naphthalene and phenanthrene forming [75, 76]. Benzene serves as a building block for CNTs by interacting with the catalyst without breaking down into atomic carbon, resulting in more curved or hunched CNT structures [75–77]. Polyaromatic hydrocarbons (PAHs) arise through benzene ring fusion and potentially react with gaseous Fe clusters. Naphthalene-like PAHs, forming a pentagon ring structure through dehydrogenation, are not a

dominant route for CNT formation [78, 79] (Fig. 8). TEM images of our results confirmed low atomic carbon levels with minimal impurities and revealed the bridged walls of CNTs, characteristic of benzene derivatives. Consequently, the inner carbon layers show slight curvatures, and the tubes themselves are also curved. Fully covered graphitic layers can deactivate iron, affecting its interaction with the tube surface during CNT growth through heterogeneous pathways [10, 80]. Carbon-encapsulated iron particles facilitate CNT growth influenced by interfacial energy and contact angle [81].

Further, ferrocene decomposition increases to generate high iron vapor density of the nucleation sites forcing to grow the CNTs upward due to the "crowding effect". In the floating catalyst process, the catalyst moves continuously with the carbon source, while its morphology is shaped by growth parameters such as flow rate, temperature, and CVD geometry [17]. These conditions drive its self-assembly and influence CNT growth, rather than relying on direct substrate deposition. In contrast, the supported catalyst method allows for more precise control during the initial deposition step, ensuring uniform distribution based on specific requirements [82]. However, the growth mechanism, whether base or tip growth, in both supported and floating catalyst methods is primarily influenced by key factors such as catalyst-substrate interactions (wettability and adhesion) and catalyst size [83–85]. In this SS-FCCVD system, the characterization data confirm that iron particles are distributed along the tube, with carbon-encapsulated iron or bare iron trapped inside the tube without disrupting its growth. However, TEM data confirmed the base growth model for CNT growth with an open-ended tube structure (Fig. 7-S).

Furthermore, iron particles are chemically stable in the total SS-FCCVD process time. As a result, small dimensions of iron particles effectively lead to the growth of very dense carbon nanotube arrays in the ceramic tube's high-temperature region. Encapsulated and bare Fe is deposited on the outer surface during the parallel growth process of CNTs. Reducing the secondary condensation reaction rate decreases the formation of PAHs. Moreover, the abundance of benzene is increased. As a result, it increases mobility and the ability to bend and interact with iron particles to grow VACNTs.

Although VACNTs grown on the reactor's inner walls can be effectively collected using a handmade scraper tool (Fig. 8-S). Additional optimization was achieved by using ceramic plates as substrates and testing different camphor/ferrocene ratios (20:1 and 15:2). These plates, cut into 4×4 cm² sections, were positioned perpendicular to the gas flow. By systematically varying the carbon source ratio, this study investigated the influence of camphor and ferrocene proportions on the growth and properties of VACNTs. A comparative analysis of
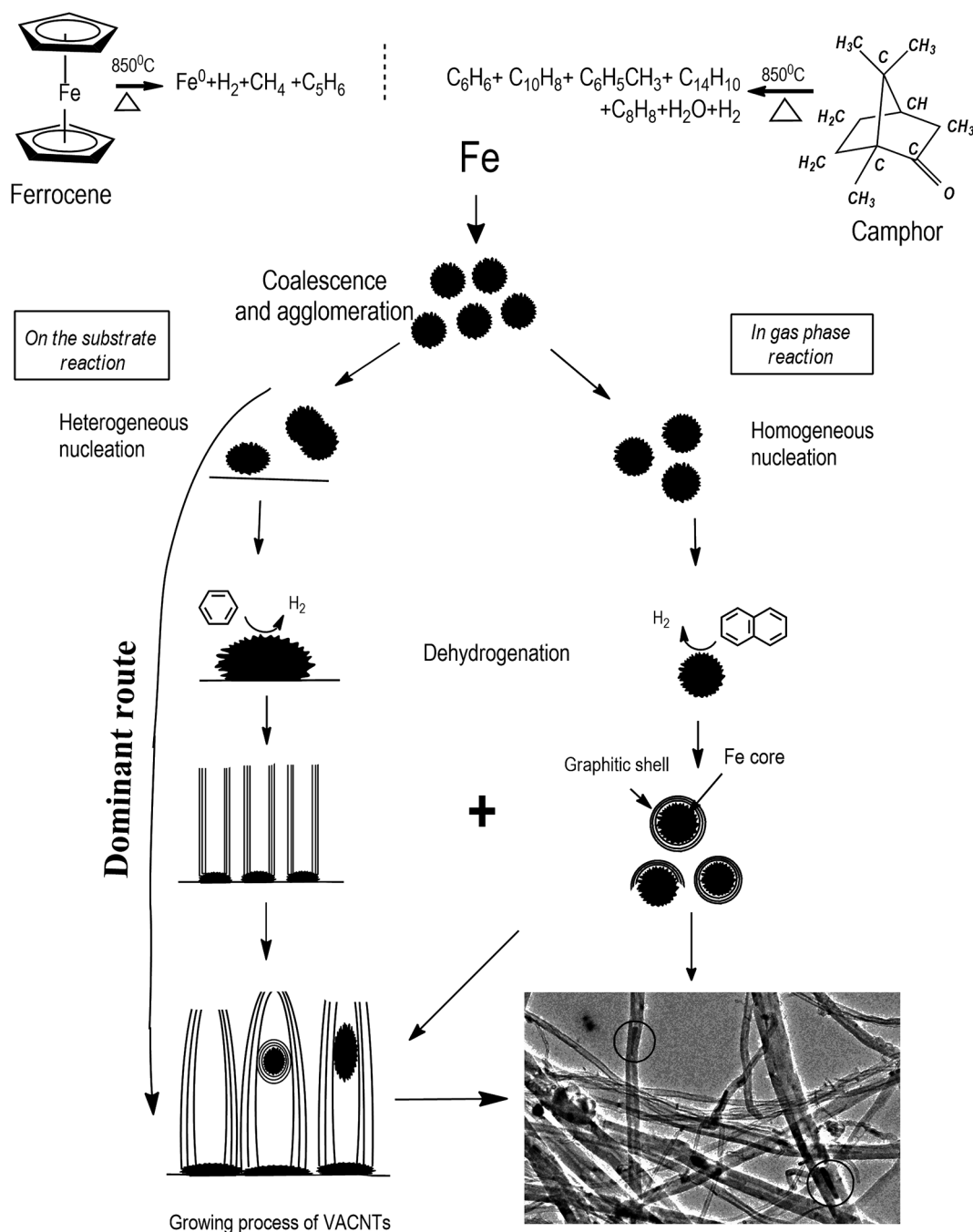
Fig. 8 The postulated mechanism for the VACNTs with carbon encapsulated iron particles from camphor and ferrocene reaction under SS-FCCVD

CNT quality, yield, and length revealed that utilizing the reactor's inner walls as a substrate resulted in more efficient VACNT growth due to the uniform deposition of high-density catalysts (Fig. 9-S). Furthermore, optimizing substrate structural properties by adjusting CVD system such as tube diameter and reaction zone's area in SS-FCCVD systems is essential for enhancing the quality and yield of VACNT growth. Notably, these nanotubes

on ceramic plate hold potential as bulk VACNT membranes for water purification.

Encapsulated catalysts with graphitic carbon offer energetic advantages and enhance iron properties, including hardness, corrosion resistance, magnetic properties, and electrical conductivity [20, 86]. Iron oxide-coated CNTs exhibit outstanding adsorption capacities for heavy metals, including chromium (Cr), lead (Pb), and zinc (Zn)

[87]. These CNTs are highly effective for direct water purification without requiring additional modifications.

Application of VACNTs

Super hydrophobic properties

The molecular mechanisms governing the manifestation of super hydrophobicity remain unresolved yet. This property is often characterized by dual surface roughness and low surface energy, assessed through contact angle (CA) measurements (superhydrophobic surface: $CA > 150^0$ and roll-off angle $< 10^0$). Various fabrication methods, such as bundling nanotubes into micro-scale pillars or regrowth, have been employed to achieve dual roughness [88, 89]. Babu et al. [90] demonstrated that freshly prepared VACNTs exhibited hydrophobicity with a contact angle of 110°–120°, while the regrowth process increased it to around 142°. Figure 9.d illustrates the contact angles of CNTs grown on silicon (Si) and alumina ceramic substrates at a carbon source loading of 17 g with a fixed camphor/ferrocene ratio of 20:1. As shown in Fig. 9, this VACNT surface shows lotus-leaf-like superhydrophobic topography [91].

The micro-patterns in VACNTs bundles create a micro-scale of roughness while the individual nanotubes contribute to the nano-scale roughness. (Fig. 9.a and e). The dual roughness creates a hierarchical structure composed of micro- and nanoscale features [92]. This structure traps a layer of air between water droplets and the surface, preventing direct contact and causing water to roll off the surface. This is a self-cleaning behavior of contaminants known as the Lotus effect [93, 94]. Nanotube orientation significantly influences surface roughness, analyzed using ImageJ with the y-axis indicating Gray Value (roughness) and the x-axis representing lateral tube distribution (Fig. 9.c and f). A uniform CNT distribution on alumina ceramic (Fig. 9.f) leads to homogeneous fluctuations in the y-scale with high surface roughness. High surface roughness correlates with low surface energy, which enhances water repellency and imparts superhydrophobic properties to the surface. On silicon plates, non-uniform CNT growth results in cluster formation and lower roughness. Adjusting the weight of camphor has been shown to improve superhydrophobicity, as demonstrated in Fig. 10-S. The inherent hydrophobicity of CNTs also contributes to their strong oleophilic properties, enabling effective oil removal [95]. This single synthesis method allows for the production of carbon nanotubes with varying morphologies, tailored for specific oil-water separation requirements.

Our study highlights the impact of CNTs orientation on collector surfaces, enabling the synthesis of diverse CNT surface morphologies by adjusting experimental
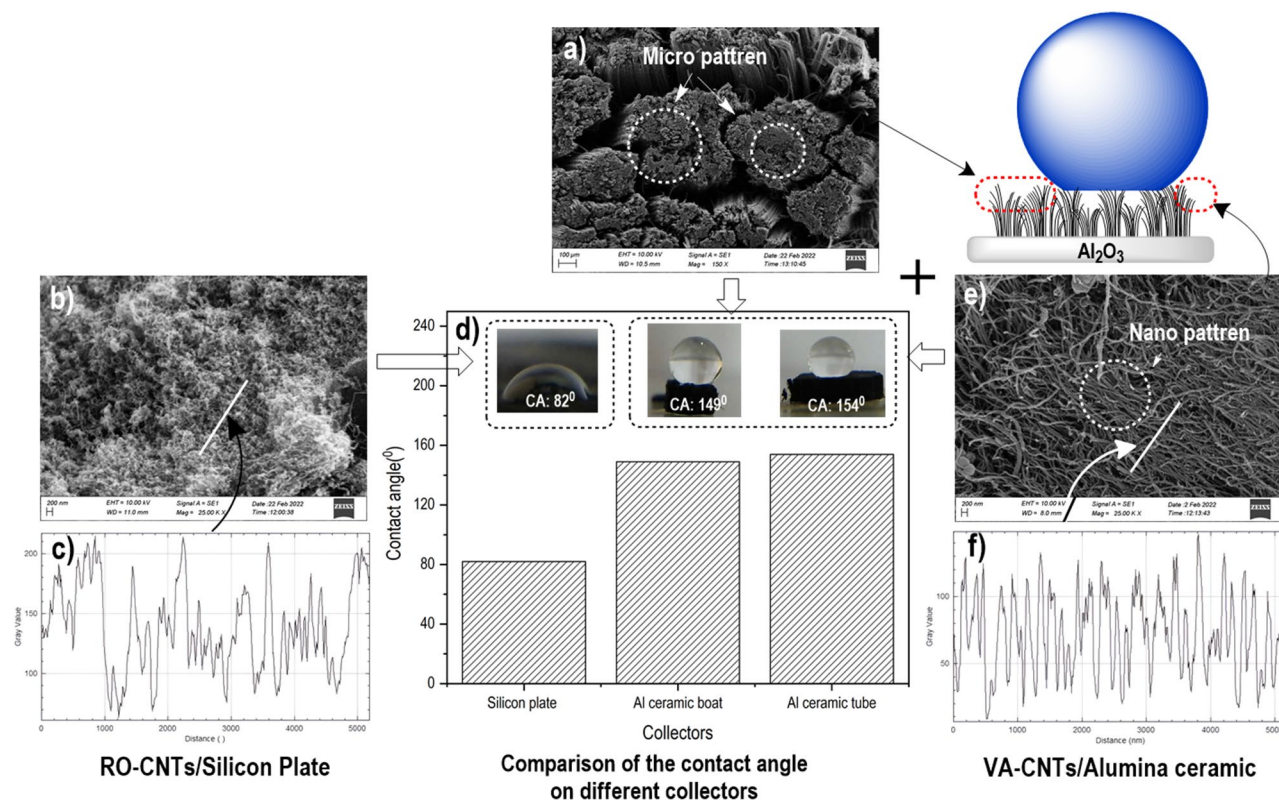

Fig. 9 SEM images in different magnifications (**a**) micro-scale and (**e**) nano-scale CNTs on alumina ceramic, (**b**) nano-scale CNTs on silicon, variation of surface roughness (gray value) across CNTs on (**c**) silicon, (**f**) alumina ceramic, and (**d**) comparison of contact angles on different collector materials
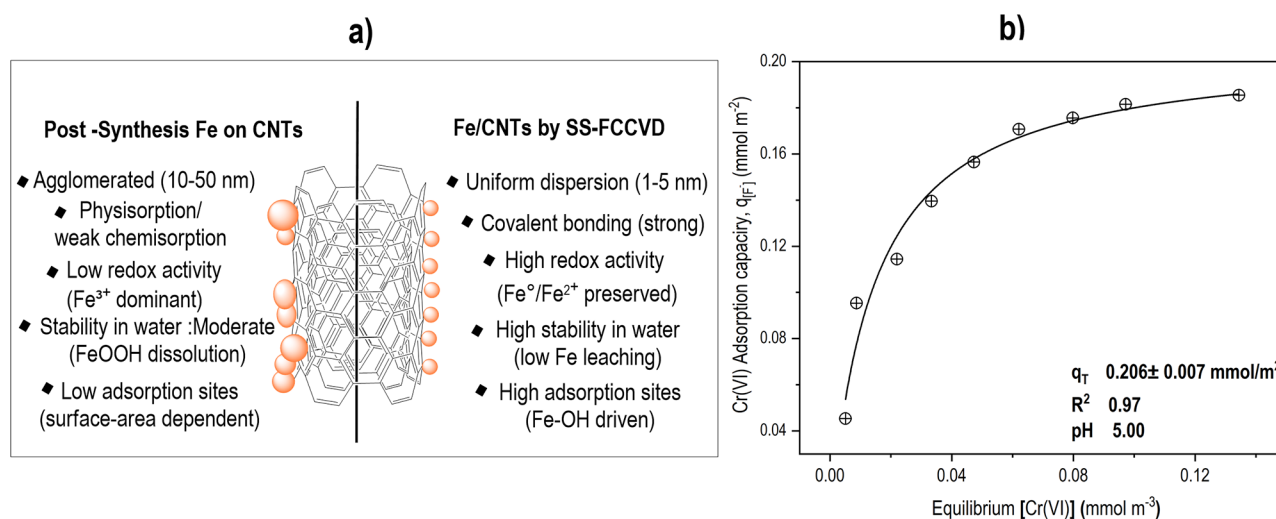
Fig. 10 **a**) The schematic illustrates as synthesis Fe/CNTs vs. post-synthesis modifications of CNTs and their impact on adsorption properties. (**b**) Adsorption isotherm on CNTs: Initial chromium concentration 1.00–10.00 mg/L, pH: 5.00, T 298 K

parameters. This exploration of various nanostructures optimizes superhydrophobicity, extending applications from oil removal, and self-cleaning to coatings with improved water repellency and other desired properties [96, 97].

Chromium(VI) adsorption

The Fe/CNT composite, with a point of zero charge (pHzpc) at approximately 5.0, promotes strong interactions with $HCrO_4^-$ ions in aqueous media [98]. This is particularly effective at pH 6, where chemical speciation analysis confirms $HCrO_4^-$ as the dominant chromium species [99]. As shown in Fig. 10. b, Cr(VI) adsorption onto CNTs within the pH range of 5–6 aligns with the Langmuir isotherm model and follows pseudo-second-order kinetics. These findings underscore the composite's exceptional efficiency and high adsorption capacity for Cr(VI) removal, positioning it as a promising material for water treatment applications.

Figure 10.a illustrates our hypothesis that hydroxylation occurs on the outer surface of CNTs, facilitated by iron centers and other surface features such as defects, kinks, and steps. Iron particulates within the CNTs may also contribute to localized hydroxyl group formation at the proximal outer sites of the CNTs. Consequently, the surface sites on the CNTs are predominantly heterogeneous but may contain localized homogeneous "islands" that enhance Cr(VI) adsorption, in agreement with the Langmuir model [100]. However, due to the limitations of the current data, more detailed measurements are necessary to fully characterize these reactive sites. Our preliminary data suggest that maximum Cr(VI) adsorption occurs at 0.0481 mM, 66.73 mM/m^2, and pH 5.0.

Despite having a relatively low BET surface area of 62.438 m^2/g, Fe/CNTs demonstrate an exceptionally high

Cr(VI) adsorption capacity of 0.206 mmol/m^2. This performance can be attributed to a synergistic combination of structural, electronic, and mechanistic factors that enhance adsorption efficiency beyond the conventional surface-area-dependent physisorption (Table 3-S). With a mean pore diameter of 8.84 nm and a low total pore volume of 0.138 cc/g, the CNTs exhibit limited porosity. Nevertheless, Cr(VI) adsorption on CNTs follows the Langmuir model, with a surface coverage of 0.828 μmol/m^2, as shown in Fig. 10.b.

During SS-FCCVD synthesis, iron from ferrocene is directly integrated into the CNT lattice or anchored as nanoparticles on its surface (Fig. 6). This in-situ integration process facilitates the formation of strong Fe–C covalent bonds, stabilizing smaller Fe nanoparticles (~1–5 nm) within the carbon matrix and preventing agglomeration (Fig. 6.C). As a result, Fe species including elemental Fe, Fe_3O_4, and FeOOH are uniformly dispersed within or on the CNT structure. This method also improves the thermal and chemical stability of the material, as the Fe nanoparticles become structurally locked within the carbon framework during high-temperature growth (850 °C).

In contrast, post-synthesis functionalization methods such as wet impregnation typically result in larger Fe particles (>20 nm) with weaker adhesion to the CNT surface and a higher tendency for agglomeration. However, the well-dispersed and stabilized Fe active centers in our synthesis play a crucial role in detoxifying pollutants by providing more reactive adsorption sites per unit area compared to oxidized CNTs or FeOOH, thus increasing efficiency [101]. Furthermore, chemical binding and redox reactions significantly contribute to the adsorption process, with Fe species facilitating the reduction of Cr(VI) to Cr(III), which is more readily adsorbed, thereby

further enhancing the overall adsorption capacity [102, 103]. To fully explore the potential of these materials, future research will employ advanced characterization techniques to assess their structural, chemical, and functional properties, which contribute to improving the adsorption capacity.

Conclusions

We employed a single-stage floating catalyst chemical vapor deposition (SS-FCCVD) method to synthesize vertically aligned carbon nanotubes (VACNTs) using camphor and ferrocene precursors without an external growth substrate. Fe is released from ferrocene and transforms into various low-coalescence species, facilitating smoother integration into surrounding structures. The use of alumina surface in the CVD reactor significantly enhanced VACNT growth, achieving record lengths. This cost-effective and scalable method offers mass production of high-quality VACNTs. The super hydrophobicity of VACNT surfaces can be tailored by adjusting precursor composition. With an impressive adsorption capacity of 0.206 mmol/m², the synthesized iron-dispersed CNTs emerge as a highly effective solution for Cr(VI) removal, ensuring outstanding efficiency in water treatment. However, the precise growth mechanism of VACNTs using SS-FCCVD requires further investigation such as confirming the growth model at the atomic scale.

Supplementary Information

The online version contains supplementary material available at https://doi.org/10.1186/s13065-025-01460-y.

Supplementary Material 1

Author contributions
Supervision (A.R. Kumarasinghe), Conceptualization (A.R. Kumarasinghe and Rohan Weerasooriya), Data curation, validation and formal analysis (Xing CHEN and L. Jayarathna), Funding acquisition, resources and Project administration (Rohan Weerasooriya and Xing CHEN), Investigation (B.V.N. Sewwandi), Visualization (Rohan Weerasooriya), Roles/Writing - original draft (B.V.N. Sewwandi), Methodology (B.V.N. Sewwandi and P. M. C. J. Bandara), Writing - review & editing (Rohan Weerasooriya).

Data availability
All data analyzed during this study are included in this published article [and its supplementary file]. Other data are available from the corresponding author upon request.

Declarations

Ethics approval and consent to participate
Not applicable.

Consent for publication
Not applicable.

Competing interests
The authors declare no competing interests.

References
1. Acharya S, Alexander R, Sahu AK, Nechiyil D, Verma A, Kaushal A, et al. Water assisted atmospheric CVD super growth of vertically aligned CNT forest for supercapacitor application. Diam Relat Mater. 2024;148(May):111481.
2. Chawla K, Cai J, Thompson D, Thevamaran R. Superior thermal transport properties of vertically aligned carbon nanotubes tailored through meso-scale architectures. Carbon N Y. 2024;216(October):118526.
3. Ge L, Wang L, Du A, Hou M, Rudolph V, Zhu Z. Vertically-aligned carbon nanotube membranes for hydrogen separation. RSC Adv. 2012;2(12):5329–36.
4. Asli NA, Shamsudin MS, Bakar SA, Mahmood MR, Abdullah S. Effect of the ratio of catalyst to carbon source on the growth of vertically aligned carbon nanotubes on nanostructured porous silicon templates. Int J Ind Chem. 2013;4(1):23.
5. Wulan PP, Silaen TPJ. Synthesis of ACNT on quartz substrate with catalytic decomposition reaction from Cinnamomum camphora by using FC-CVD method. AIP Conf Proc. 2017;1840.
6. Weissker U, Hampel S, Leonhardt A, Büchner B. Carbon nanotubes filled with ferromagnetic materials. Mater (Basel). 2010;3(8):4387–427.
7. Roumeli E, Diamantopoulou M, Serra-Garcia M, Johanns P, Parcianello G, Daraio C. Characterization of vertically aligned carbon nanotube forests grown on stainless steel surfaces. Nanomaterials. 2019;9(3):18–25.
8. Tewari A, Sharma SC. Effect of different carrier gases and their flow rates on the growth of carbon nanotubes. Phys Plasmas. 2015;22(4).
9. Xie S, Song L, Ci L, Zhou Z, Dou X, Zhou W, et al. Controllable Preparation and properties of single-/double-walled carbon nanotubes. Sci Technol Adv Mater. 2005;6(7):725–35.
10. Xu Y, Ma Y, Liu Y, Feng S, He D, Haghi-Ashtiani P, et al. Evolution of nanoparticles in the gas phase during the floating chemical vapor deposition synthesis of carbon nanotubes. J Phys Chem C. 2018;122(11):6437–46.
11. Charon E, Pinault M, Mayne-L'Hermite M, Reynaud C. One-step synthesis of highly pure and well-crystallized vertically aligned carbon nanotubes. Carbon N Y. 2021;173:758–68.
12. Hou PX, Zhang F, Zhang L, Liu C, Cheng HM. Synthesis of carbon nanotubes by floating catalyst chemical vapor deposition and their applications. Adv Funct Mater. 2022;32(11).
13. Yoshihara K, Honda SI, Lee JG, Mori H, Oura K, Katayama M. High-density growth of vertically aligned carbon nanotubes with high linearity by catalyst preheating in acetylene atmosphere. Jpn J Appl Phys. 2008;47(4 PART 1):1941–3.
14. Ramirez A, Royo C, Latorre N, Mallada R, Tiggelaar RM, Monzón A. Unraveling the growth of vertically aligned multi-walled carbon nanotubes by chemical vapor deposition. Mater Res Express. 2014;1(4):045604.
15. Lubej M, Plazl I. Theoretical and experimental study of iron catalyst Preparation by chemical vapor deposition of ferrocene in air. Chem Eng J. 2014;242:306–12.
16. Sehrawat M, Rani M, Sharma S, Bharadwaj S, Falzon BG, Singh BP. Floating catalyst chemical vapour deposition (FCCVD) for direct spinning of CNT aerogel: A review. Carbon N Y. 2024;219(November 2023):118747.
17. Kaushal A, Alexander R, Prakash J, Dasgupta K. Engineering challenges and innovations in controlled synthesis of CNT fiber and fabrics in floating catalyst chemical vapor deposition (FC-CVD) process. Diam Relat Mater. 2024;148(March):111474.
18. Lee SH, Park J, Park JH, Lee DM, Lee A, Moon SY, et al. Deep-injection floating-catalyst chemical vapor deposition to continuously synthesize carbon nanotubes with high aspect ratio and high crystallinity. Carbon N Y. 2021;173:901–9.

19. Kinoshita T, Karita M, Nakano T, Inoue Y. Two step floating catalyst chemical vapor deposition including in situ fabrication of catalyst nanoparticles and carbon nanotube forest growth with low impurity level. Carbon N Y. 2019;144:152–60.

20. Kapoor A, Singh N, Dey AB, Nigam AK, Bajpai A. 3d transition metals and oxides within carbon nanotubes by Co-Pyrolysis of metallocene & Camphor: high filling efficiency and Self-Organized structures. Carbon N Y. 2018;132:733–45.

21. Osorio AG, Bergmann CP. Effect of surface area of substrates aiming the optimization of carbon nanotube production from ferrocene. Appl Surf Sci. 2013;264:794–800.

22. Khare RA, Agarwal US, Thaliyil VS. Process of preparation of carbon nanotubes [Internet]. 2014. Available from: https://patentscope.wipo.int/search/en/detail.jsf?docId=WO2014203280%26_cid=P11-M2LIAT-83968-1

23. Mosallanejad S, Dlugogorski BZ, Kennedy EM, Stockenhuber M. On the chemistry of iron oxide supported on γ-Alumina and silica catalysts. ACS Omega. 2018;3(5):5362–74.

24. Shahzad MI, Giorcelli M, Perrone D, Virga A, Shahzad N, Jagdale P et al. Growth of vertically aligned multiwall carbon nanotubes columns. J Phys Conf Ser. 2013;439(1).

25. Gheitaghy AM, Ghaderi A, Vollebregt S, Ahmadi M, Wolffenbuttel R, Zhang GQ. Infrared absorbance of vertically-aligned multi-walled CNT forest as a function of synthesis temperature and time. Mater Res Bull. 2020;126(February).

26. Sepahvand S, Safaei P, Sanaee Z. Growth of carbon nano tubes on copper substrate suitable for lithium ion battery anode. Procedia Mater Sci. 2015;11(2013):634–8.

27. Braga TS, Vieira NCS, Antonelli E, Rosa FM, Donadon MV, Corat EJ. Development and study of low-cost VACNT/PDMS stretchable and resistive strain sensor. Sens Actuators Phys. 2020;315(June):112358.

28. Cao PJ, Zhu DL, Liu WJ, Ma XC. The effect of substrate morphology on the diameter distribution of carbon nanotubes grown on silica and ceramic substrates. Mater Lett. 2007;61(8–9):1899–903.

29. Choi H, Gong J, Lim Y, Im KH, Jeon M. Effects of the electrical conductivity and orientation of silicon substrate on the synthesis of multi-walled carbon nanotubes by thermal chemical vapor deposition. Nanoscale Res Lett. 2013;8(1):1.

30. Sharma P, Pavelyev V, Kumar S, Mishra P, Tripathi SSI. Analysis on the synthesis of vertically aligned carbon nanotubes: growth mechanism and techniques. J Mater Sci Mater Electron. 2020;31:4399–443.

31. Lettiere BR, Chazot CAC, Cui K, John Hart A. High-Density carbon nanotube forest growth on copper foil for enhanced thermal and electrochemical interfaces. ACS Appl Nano Mater. 2020;3(1):77–83.

32. Thyssen VV, Maia TA, Assaf EM. Cu and Ni catalysts supported on γ-Al2O3 and SiO2 assessed in glycerol steam reforming reaction. J Braz Chem Soc. 2015;26(1):22–31.

33. Morco SR, Jensen BD, Bowden AE. Curvature-induced defects on carbon-infiltrated carbon nanotube forests. RSC Adv. 2022;12(4):2115–22.

34. Shafa M, Wang Z, Naz MY, Akbar S, Farooq MU, Ghaffar A. Morphology and photoresponse of crystalline antimony film grown on mica by physical vapor deposition. Mater Sci Pol. 2016;34(3):591–6.

35. Morgan GS, Lucas SG. Chemical Vapor deposition. In: Bulletin of the American Museum of Natural History. 2003. pp. 269–320.

36. Nasibulin AG, Moisala A, Jiang H, Kauppinen EI. Carbon nanotube synthesis from alcohols by a novel aerosol method. J Nanoparticle Res. 2006;8(3–4):465–75.

37. Gomes DJC, De Souza NC, Silva JR. Using a monocular optical microscope to assemble a wetting contact angle analyser. Meas J Int Meas Confed. 2013;46(9):3623–7.

38. Xu S, Man B, Jiang S, Yue W, Yang C, Liu M et al. Direct growth of graphene on quartz substrates for label-free detection of adenosine triphosphate. Nanotechnology. 2014;25(16).

39. Musso S, Porro S, Rovere M, Giorcelli M, Tagliaferro A. Fluid dynamic analysis of gas flow in a thermal-CVD system designed for growth of carbon nanotubes. J Cryst Growth. 2008;310(2):477–83.

40. Bhattacharjee A, Rooj A, Roy D, Roy A. Thermal decomposition study of ferrocene [(C5H5)2Fe]. J Exp Phys. 2014;2014:2333–9721.

41. Çelik Y, Suvaci E, Weibel A, Peigney A, Flahaut E. Texture development in Fe-doped alumina ceramics via templated grain growth and their application to carbon nanotube growth. J Eur Ceram Soc. 2013;33(6):1093–100.

42. Wan HJ, Wu BS, Zhang CH, Xiang HW, Li YW, Xu BF, et al. Study on Fe-Al2O3 interaction over precipitated iron catalyst for Fischer-Tropsch synthesis. Catal Commun. 2007;8(10):1538–45.

43. Mosallanejad S, Dlugogorski BZ, Kennedy EM, Stockenhuber M. Adsorption of 2-Chlorophenol on the surface of Silica- and Alumina-Supported iron oxide: an FTIR and XPS study. ChemCatChem. 2017;9(3):481–91.

44. Cao JM. Selective growth of carbon Nantoubes on SiO 2 /Si substrate. Appl Surf Sci. 2006;253(5):2460–4.

45. Futaba DN, Hata K, Namai T, Yamada T, Mizuno K, Hayamizu Y, et al. 84% catalyst activity of water-assisted growth of single walled carbon nanotube forest characterization by a statistical and macroscopic approach. J Phys Chem B. 2006;110(15):8035–8.

46. Atthipalli G. Growth of aligned carbon Naotubes on copper substates. J Controlled Release. 2011.

47. N HS, MK Y, L B. K, M S, M B, Synthesis of carbon nanotubes for Oil-water interfacial tension reduction. Oil Gas Res. 2015;1(1).

48. Okotrub AV, Gorodetskiy DV, Gusel'nikov AV, Kondranova AM, Bulusheva LG, Korabovska M et al. Distribution of iron nanoparticles in arrays of vertically aligned carbon nanotubes grown by chemical vapor deposition. Mater (Basel). 2022;15(19).

49. Shariatzadeh SMR, Salimi M, Fathinejad H, Joshaghani AH. Nanostructured α-Fe2O3: solvothermal synthesis, characterization, and effect of synthesis parameters on structural properties. Int J Eng Trans B Appl. 2022;35(6):1186–92.

50. Hansson J, Nylander A, Flygare M, Svensson K, Ye L, Nilsson T et al. Effects of high temperature treatment of carbon nanotube arrays on graphite: increased crystallinity, anchoring and inter-tube bonding. Nanotechnology. 2020;31(45).

51. Marshall CP, Marshall AO. Hematite and carbonaceous materials in geological samples: A cautionary Tale. Spectrochim Acta - Part Mol Biomol Spectrosc. 2011;80(1):133–7.

52. Hai NH, Phu ND, Luong NH, Chau N, Chinh HD, Hoang LH, et al. Mechanism for sustainable magnetic nanoparticles under ambient conditions. J Korean Phys Soc. 2008;52(5):1327–31.

53. Kouotou PM, Tian ZY, Vieker H, Beyer A, Gölzhäuser A, Kohse-Höinghaus K. Selective synthesis of α-Fe2O3 thin films and effect of the deposition temperature and lattice oxygen on the catalytic combustion of Propene. J Mater Chem A. 2013;1(35):10495–504.

54. Owens FJ, Orosz J. Effect of nanosizing on lattice and Magnon modes of hematite. Solid State Commun. 2006;138(2):95–8.

55. Colomban P. Potential and Drawbacks of Raman (Micro)spectrometry for the Understanding of Iron and Steel Corrosion. In: New Trends and Developments in Automotive System Engineering. 2011.

56. Antunes EF, De Resende VG, Mengui UA, Cunha JBM, Corat EJ, Massi M. Analyses of residual iron in carbon nanotubes produced by camphor/ferrocene pyrolysis and purified by high temperature annealing. Appl Surf Sci. 2011;257(18):8038–43.

57. Wu HC, Hong CT, Chiu HT, Li YY. Continuous synthesis of carbon spheres by a non-catalyst vertical chemical vapor deposition. Diam Relat Mater. 2009;18(4):601–5.

58. Deshmukh AA, Mhlanga SD, Coville NJ. Carbon spheres. Mater Sci Eng R Rep. 2010;70(1–2):1–28.

59. Wang S, Ni L, Fu X, Duan D, Xu J, Gao X. A sulfated polysaccharide from Saccharina Japonica suppresses LPS-Induced inflammation both in a macrophage cell model via blocking MAPK/NF-κB signal pathways in vitro and a zebrafish model of embryos and larvae in vivo. Mar Drugs. 2020;18(12):593.

60. Petersen EJ, Lam T, Gorham JM, Scott KC, Long CJ, Stanley D, et al. Methods to assess the impact of UV irradiation on the surface chemistry and structure of multiwall carbon nanotube epoxy nanocomposites. Carbon N Y. 2014;69(March 2019):194–205.

61. Zhong L, Yun K. Graphene oxide-modified ZnO particles: synthesis, characterization, and antibacterial properties. Int J Nanomed. 2015;10:79–92.

62. Awale RJ, Ali FB, Azmi AS, Puad NIM, Anuar H, Hassan A. Enhanced flexibility of biodegradable polylactic acid/starch blends using epoxidized palm oil as plasticizer. Polym (Basel). 2018;10(9).

63. Kumar A, Khandelwal M, Gupta SK, Kumar V, Rani R. Fourier transform infrared spectroscopy: Data interpretation and applications in structure elucidation and analysis of small molecules and nanostructures. Data Processing Handbook for Complex Biological Data Sources. Elsevier Inc.; 2019. 77–96 p.

64. Nawaz T, Zulfiqar S, Sarwar MI, Iqbal M. Synthesis of Diglycolic acid functionalized core-shell silica coated Fe3O4 nanomaterials for magnetic extraction of Pb(II) and Cr(VI) ions. Sci Rep. 2020;10(1):1–14.

65. Ortega KF, Arrigo R, Frank B, Schlögl R, Trunschke A. Acid-Base properties of N-Doped carbon nanotubes: A combined Temperature-Programmed

desorption, X-ray photoelectron spectroscopy, and 2-Propanol reaction investigation. Chem Mater. 2016;28(19):6826–39.

66. Pirlot C, Mekhalif Z, Fonseca A, Nagy JB, Demortier G, Delhalle J. Surface modifications of carbon nanotube/polyacrylonitrile composite films by proton beams. Chem Phys Lett. 2003;372(3–4):595–602.

67. Yang JY, Jiang XY, Jiao FP, Yu JG. The oxygen-rich pentaerythritol modified multi-walled carbon nanotube as an efficient adsorbent for aqueous removal of Alizarin yellow R and Alizarin red S. Appl Surf Sci. 2018;436:198–206.

68. Korusenko PM, Nesov SN, Bolotov VV, Povoroznyuk SN, Pushkarev AI, Knyazev EV. Changes in the chemical state and concentration of iron in carbon nanotubes obtained by the CVD method and exposed to pulsed ion irradiation. Phys Solid State. 2017;59(10):2045–52.

69. Qureshi MI, Patel F, Al-Baghli N, Abussaud B, Tawabini BS, Laoui T. A comparative study of Raw and metal oxide impregnated carbon nanotubes for the adsorption of hexavalent chromium from aqueous solution. Bioinorg Chem Appl. 2017;2017(Vi).

70. Pełech I, Pełech R, Narkiewicz U, Moszyński D, Jdrzejewska A, Witkowski B. Chlorination of carbon nanotubes obtained on the different metal catalysts. J Nanomater. 2013;2013.

71. Edwards ER, Antunes EF, Botelho EC, Baldan MR, Corat EJ. Evaluation of residual iron in carbon nanotubes purified by acid treatments. Appl Surf Sci. 2011;258(2):641–8.

72. Gökstorp FKA, Juniper MP. Flow simulations including iron nanoparticle nucleation, growth and evaporation for floating catalyst Cnt production. Catalysts. 2020;10(12):1–17.

73. Castro C, Pinault M, Coste-Leconte S, Porterat D, Bendiab N, Reynaud C, et al. Dynamics of catalyst particle formation and multi-walled carbon nanotube growth in aerosol-assisted catalytic chemical vapor deposition. Carbon N Y. 2010;48(13):3807–16.

74. Chen DR, Chitranshi M, Schulz M, Shanov V. A review of three major factors controlling carbon nanotubes synthesis from the floating catalyst chemical vapor deposition. Nano Life. 2019;09(04):1930002.

75. Wulan PPDK, Fathony A, Ulfa AS. Utilization of Camphor as an alternative carbon source for the synthesis of carbon nanotubes using floating catalyst. J Phys Conf Ser. 2019;1349(1).

76. Musso S, Zanetti M, Giorcelli M, Tagliaferro A, Costa L. Gas chromatography study of reagent degradation during chemical vapor deposition of carbon nanotubes. J Nanosci Nanotechnol. 2009;9(6):3593–8.

77. Kumar M, Ando Y. A simple method of producing aligned carbon nanotubes from an unconventional precursor - Camphor. Chem Phys Lett. 2003;374:521–6.

78. Mackie CJ, Peeters E, Bauschlicher CW, Cami J. Characterizing the infrared spectra of small, neutral, fully dehydrogenated polycyclic aromatic hydrocarbons. Astrophys J. 2015;799(2).

79. Sewwandi BVN, Kumarasinghe AR, Wu Z, Bandara PMCJ, Jayarathne L, Bandara A, et al. Size-tunable graphitized carbon spheres for water defluoridation. Colloids Surf Physicochem Eng Asp. 2023;670(May):1–12.

80. Harish V, Ansari MM, Tewari D, Gaur M, Yadav AB, García-Betancourt ML, et al. Nanoparticle and nanostructure synthesis and controlled growth methods. Nanomaterials. 2022;12(18):1–30.

81. Orbán B, Höltzl T. The promoter role of sulfur in carbon nanotube growth. Dalt Trans. 2022;51(24):9256–64.

82. Yu Z, Chen D, Tøtdal B, Holmen A. Effect of catalyst Preparation on the carbon nanotube growth rate. Catal Today. 2005;100(3–4):261–7.

83. Gohier A, Ewels CP, Minea TM, Djouadi MA. Carbon nanotube growth mechanism switches from tip- to base-growth with decreasing catalyst particle size. Carbon N Y. 2008;46(10):1331–8.

84. Ayillath Kutteri D, Wang IW, Samanta A, Li L, Hu J. Methane decomposition to tip and base grown carbon nanotubes and COx-free H2 over mono- and bimetallic 3d transition metal catalysts. Catal Sci Technol. 2018;8(3):858–69.

85. Venkataraman A, Amadi EV, Chen Y, Papadopoulos C. Carbon nanotube assembly and integration for applications. Nanoscale Res Lett. 2019;14(1).

86. Fronczak M, Łabędź O, Kaszuwara W, Bystrzejewski M. Corrosion resistance studies of carbon-encapsulated iron nanoparticles. J Mater Sci. 2018;53(5):3805–16.

87. Fouda-Mbanga BG, Onotu OP, Olushuyi CI, Nthwane YB, Nyoni B, Zikhona TN. Application of metallic oxide coated carbon nanoparticles in adsorption of heavy metals and reusability for latent fingerprint detection: A review. Hybrid Adv. 2024;6:100248.

88. Zhang Y, Stan L, Xu P, Wang HL, Doorn SK, Htoon H, et al. A double-layered carbon nanotube array with super-hydrophobicity. Carbon N Y. 2009;47(14):3332–6.

89. Zhang L, Resasco DE. Single-walled carbon nanotube pillars: A superhydrophobic surface. Langmuir. 2009;25(8):4792–8.

90. Babu DJ, Mail M, Barthlott W, Schneider JJ. Superhydrophobic vertically aligned carbon nanotubes for biomimetic air retention under water (Salvinia Effect). Adv Mater Interfaces. 2017;4(13):1–6.

91. Wang F, Wang L, Wu H, Pang J, Gu D, Li S. A lotus-leaf-like SiO2 superhydrophobic bamboo surface based on soft lithography. Colloids Surf Physicochem Eng Asp. 2017;520:834–40.

92. Yoon Y, Kim D, Lee JB. Hierarchical micro/nano structures for super-hydrophobic surfaces and super-lyophobic surface against liquid metal. Micro Nano Syst Lett. 2014;2(1):1–18.

93. Van Hooijdonk E, Bittencourt C, Snyders R, Colomer JF. Functionalization of vertically aligned carbon nanotubes. Beilstein J Nanotechnol. 2013;4(1):129–52.

94. Noamani S, Niroomand S, Rastgar M, Sadrzadeh M. Carbon-based polymer nanocomposite membranes for oily wastewater treatment. Npj Clean Water. 2019;2(1):1–14.

95. Babar Z, Bin, Rizwan K, Munir S. Multifunctional smart Nano-membranes for the removal of Oil-Based pollutants from marine sources: A tool for sustainable environment. Water Air Soil Pollut. 2024;235(1):1–27.

96. Sethi S, Dhinojwala A. Superhydrophobic conductive carbon nanotube coatings for steel. Langmuir. 2009;25(8):4311–3.

97. Belsanti L, Ogihara H, Mahanty S, Luciano G. Electrochemical behaviour of superhydrophobic coating fabricated by spraying a carbon nanotube suspension. Bull Mater Sci. 2015;38(2):579–82.

98. Marques Neto J, de O, Bellato CR, de Silva D. Iron oxide/carbon nanotubes/chitosan magnetic composite film for chromium species removal. Chemosphere. 2019;218:391–401.

99. García-Sosa I, Olguín MT. Comparison between the Cr(VI) adsorption by hydrotalcite and hydrotalcite-Gibbsite compounds. Sep Sci Technol. 2015;50(17):2631–8.

100. Panczyk T, Rudzinski W. Effects of surface heterogeneity of carbon nanotubes in adsorption of colloid nanoparticles studied by means of computer simulations. Adsorption. 2013;19(2–4):611–8.

101. Barakat MA, Al-Ansari AM, Kumar R. Synthesis and characterization of Fe-Al binary oxyhydroxides/ MWCNTs nanocomposite for the removal of Cr(VI) from aqueous solution. J Taiwan Inst Chem Eng. 2016;63:1–9.

102. Kumar ASK, Jiang SJ, Tseng WL. Effective adsorption of chromium(vi)/Cr(iii) from aqueous solution using ionic liquid functionalized multiwalled carbon nanotubes as a super sorbent. J Mater Chem A. 2015;3(13):7044–57.

103. Kang Z, Jia X, Ma X, Wen D. Modelling and prediction of Fe/MWCNT nanocomposites for hexavalent chromium reduction. Processes. 2023;11(12):3271.

Publisher's note